Medical Image Analysis 39 (2017) 56–77

Contents lists available at ScienceDirect

Medical Image Analysis

journal homepage: www.elsevier.com/locate/media

Maximum likelihood estimation of cardiac fiber bundle orientation from arbitrarily spaced diffusion weighted images

Andreas Nagler[a], Cristóbal Bertoglio[b,a,*], Christian T. Stoeck[c,d], Sebastian Kozerke[c,d], Wolfgang A. Wall[a]

[a] Institute for Computational Mechanics, Technical University of Munich, Germany
[b] Center for Mathematical Modeling, Universidad de Chile, Chile
[c] Institute for Biomedical Engineering, University and ETH Zurich, Switzerland
[d] Division of Imaging Sciences and Biomedical Engineering, King's College London, UK

ARTICLE INFO

Article history:
Received 4 March 2016
Revised 6 March 2017
Accepted 21 March 2017
Available online 4 April 2017

Keywords:
Cardiac fibers
Cardiac diffusion tensor imaging
Maximum likelihood estimation
Motion correction

ABSTRACT

We propose an estimation scheme for local fiber bundle direction in the left ventricle directly from gray values of arbitrarily spaced cardiac diffusion weighted images (DWI). The approach is based on a parametric and space-dependent mathematical representation of the myocardial fiber bundle orientation and hence the diffusion tensor (DT) for the ventricular geometry. By solving a nonlinear inverse problem derived from a maximum likelihood estimator, the degrees of freedom of the fiber and DT model can be estimated from the measured gray values of the DWIs. The continuity of the DT model allows to relax the restriction to the individual DWIs to match spatially like for voxelwise DT calculation. Hence, the spatial misalignment between image slices with different diffusion encoding directions, that is encountered in-vivo cardiac imaging practice can be integrated into the estimation scheme. This feature results then in a negligible impact of the spatial misalignment on the reconstructed solution. We illustrate the methodology using synthetic data and compare it against a previously reported fiber bundle reconstruction technique. To show the potential for real data, we also present results for multi-slice data constructed from ex-vivo cardiac diffusion weighted measurements in both mono- and bi-ventricular configurations.

1. Introduction

Diffusion Weighted Magnetic Resonance Imaging (DW-MRI) is capable to measure the fiber architecture of tissues non-invasively (Basser et al., 1994). Based on the relation between gray values within a pulsed gradient spin echo experiment (Stejskal and Tanner, 1965):

$$g^{(i)} = g^{(0)} \exp\left(-\boldsymbol{b}^{(i)\mathsf{T}} \mathcal{D} \boldsymbol{b}^{(i)}\right) \tag{1}$$

the tissue anisotropy information – represented as diffusion tensor $\mathcal{D} \in \mathbb{R}^{3\times3}$ – can be connected with the diffusion encoding directions $\boldsymbol{b}^{(0)}, \boldsymbol{b}^{(1)}, \dots \in \mathbb{R}^3$ and the measured gray values $g^{(0)}, g^{(1)}, \dots \in \mathbb{R}^+$. Since the diffusion tensor is symmetric positive definite, at least 6 gray value measurements plus one non-weighted reference measurement are required to estimate all diffusion tensor components, but usually between 10 to 20 are acquired in order to compensate for measurement noise. It has been shown, that the diffusion tensor's principal eigenvector correlates well with the tissue structure given single fiber populations within the region of interest (Scollan et al., 1998; Hsu et al., 1998).

Full three-dimensional measurements of the myocardial fiber structure through DW-MRI suffer from long scan times. Hence, it was mainly applied to *ex-vivo* heart samples, see e.g. (Lombaert et al., 2012) and references therein.

Recently, *in-vivo* DW-MRI acquisitions in a limited number of slices along the heart were reported (Gamper et al., 2007; Nguyen et al., 2013; Nielles-Vallespin et al., 2013; Stoeck et al., 2015; Moulin et al., 2015). Hence, a three-dimensional reconstruction of the fibers from sparsely distributed DW-MRI data is needed, which has to deal not only with low signal-to-noise ratios, but also with the spatial mismatch of the diffusion weighted images (DWIs).

The image slices for cardiac DW-MRI are typically acquired at fixed positions with respect to the reference frame of the MR-scanner. Nevertheless, motion of the heart due to different breathing levels and eddy current effects implies that every DWI corresponding to each gradient encoding direction for a given slice has a different location with respect the heart itself.

* Corresponding author.
E-mail addresses: nagler@lnm.mw.tum.de (A. Nagler), cbertoglio@dim.uchile.cl (C. Bertoglio), stoeck@biomed.ee.ethz.ch (C.T. Stoeck), kozerke@biomed.ee.ethz.ch (S. Kozerke), wall@lnm.mw.tum.de (W.A. Wall).

http://dx.doi.org/10.1016/j.media.2017.03.005
1361-8415/

Recently in Toussaint et al. (2013), a regularized tensor interpolation method, based on curvilinear coordinates, was proposed for reconstructing the left ventricular fiber architecture from a set of in-vivo DWI-slices. Since its starting point is a voxelwise linear estimation of the diffusion tensor, it relies on the perfect spatial matching of the DWIs with respect to the ventricular geometry, which cannot be achieved in vivo.

To reduce spatial mismatch, respiratory gating (Sachs et al., 1994) with small acceptance windows are used during in-vivo acquisition, therefore significantly prolonging total scan duration. Specifically, current acquisition consists in 6 short axis slices using about $\pm$ 2.5 mm for acceptance window, implying 30–50% of data acceptance rate (Nielles-Vallespin et al., 2013; Nguyen et al., 2013; von Deuster et al., 2015).

The goal of this work is to propose a methodology that is able to reconstruct the myocardial fiber orientation from DW-MRI data by directly handling arbitrarily spaced DWIs. A reconstruction technique that may robustly deal with larger respiratory gating windows would allow to reduce imaging time, improving the chance of diffusion MRI to be applied in clinical studies.

To achieve this, we build a continuous and parametrizable model of the cardiac fiber bundles angles, and therefore of the diffusion tensor. We can then adapt the fiber angle field in an individual-specific manner by estimating the degrees of freedom of such model from the measured DWIs using a maximum likelihood approach. We can therefore relax the restriction to the individual DWIs to match spatially, since the continuous representation of the fiber architecture allows to "glue" the information coming from different spatial locations. A very preliminary version of this method using solely a simple prolate spheroid geometry was reported in Nagler et al. (2015). In this article, we introduce several additional and crucial methodological developments from the model selection and inverse problems fields, as well with more extended examples with synthetic data and with real DW-MRI measurements. In all the presented tests, the superior performance of our approach with respect to the state-of-the-art curvilinear tensor interpolation becomes explicit.

The rest of the paper is organized as follows. Section 2 justifies and describes the proposed diffusion tensor model and introduces the estimation formulation. In Section 3, we exemplify the method using a synthetic fiber data set on a deformed prolate spheroid geometry, and we compare the performance of the proposed method against the curvilinear tensor-interpolation of Toussaint et al. (2013). In Section 4, the applicability of the method on real DW-MRI measurements is shown by using multi-slice diffusion images subsampled from a high-resolution ex-vivo data set. Finally, a more detailed discussion of the results and some perspectives are presented in Sections 5.

2. Methods

In this section, we first describe the mathematical model of the diffusion tensor (DT) and the parametrizable fiber angle fields. Next, we introduce classical model selection concepts in order to systematically find a suitable parametrization for a given amount of noisy data. This allows to choose a reasonable number of parameters of the model to avoid overfitting. Finally, we detail the maximum likelihood fiber estimator algorithm used later in the numerical examples. Throughout this article, we will use convention that scalar, vector or matrix/tensor quantities will have normal, bold and calligraphic font, respectively.

2.1. The diffusion tensor model

We start from the assumption that epicardial and endocardial surfaces of the left ventricular geometry are available, from which

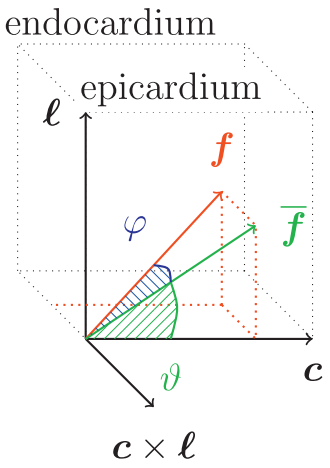

Fig. 1. Fiber angles definition.

a three-dimensional tetrahedral mesh discretization of the domain $\Omega \subset \mathbb{R}^3$ with vertices $\boldsymbol{x}_1, \ldots, \boldsymbol{x}_p \in \Omega$ has been constructed, with p the number of vertices of the computational mesh. Then, we define for every point within Ω the transverse isotropic DT model of the form:

$$\mathcal{D}(\vartheta, \varphi, \boldsymbol{\lambda}, \boldsymbol{c}, \boldsymbol{\ell}) = (\lambda_1 - \lambda_2)[\boldsymbol{f}(\vartheta, \varphi, \boldsymbol{c}, \boldsymbol{\ell}) \otimes \boldsymbol{f}(\vartheta, \varphi, \boldsymbol{c}, \boldsymbol{\ell})] + \lambda_2 \mathcal{I}. \tag{2}$$

where $\mathcal{I}$ is the identity matrix. The values $\boldsymbol{\lambda} = [\lambda_1, \lambda_2] > 0$ are the *diffusivities* in fiber and cross-fiber direction, respectively. The fiber directions are defined as:

$$\boldsymbol{f}(\vartheta, \varphi, \boldsymbol{c}, \boldsymbol{\ell}) = \cos(\vartheta)\cos(\varphi)\boldsymbol{c} + \sin(\vartheta)\cos(\varphi)\boldsymbol{\ell} + \sin(\varphi)\boldsymbol{c} \times \boldsymbol{\ell} \tag{3}$$

where $\vartheta, \varphi : \Omega \to \mathbb{R}$ are the local *helix* and *transverse angle* of the fibers and $\boldsymbol{c}, \boldsymbol{\ell} : \Omega \to \mathbb{R}^3$ the local *circumferential* and *long-axial direction*, respectively. Furthermore, $[\boldsymbol{c}, \boldsymbol{\ell}, \boldsymbol{c} \times \boldsymbol{\ell}]$ forms an orthonormal system for all $\boldsymbol{x} \in \Omega$. A graphical sketch of the fiber angle definition is given in Fig. 1.

2.2. The parametrizable fiber angle model

The next (and key) step in the fiber estimation framework is to build a continuous, but parametrizable DT model, which is based on a spatial parametrization of the cardiac fiber angles. The degrees-of-freedom (DOF) of the fiber angle fields will be adapted for each data set by estimating the DOF of such model from the measured DWIs. In the following lines we describe how we represent this model for a fixed number of DOF.

We assume that the helix and transverse fiber angles distributions are discretized by piecewise continuous fields over "surface patches", see Fig. 2. These patches are based on regular partitions of the heart surface and do not necessarily agree with the classical AHA partitions. The angle fields are then characterized by a set of DOF $\boldsymbol{\Theta} \in]-90^\circ, 90^\circ[^{\kappa_h}$, $\boldsymbol{\Phi} \in]-90^\circ, 90^\circ[^{\kappa_t}$, $\kappa_h, \kappa_t \in \mathbb{N}$, respectively, corresponding to the angle values at the vertices of the patches, see Fig. 2(b). The criteria for the adequate number of partitions (and hence of DOF) will be introduced in Section 2.3.

We assume therefore that the following relation holds for each vertex of the computational mesh $\boldsymbol{x}_j$:

$$\vartheta(\boldsymbol{x}_j) = \tau(\beta, t(\boldsymbol{x}_j))\mathcal{Z}_j^{k_h}\boldsymbol{\Theta}, \quad \varphi(\boldsymbol{x}_j) = \mathcal{Z}_j^{k_t}\boldsymbol{\Phi} \tag{4}$$

where the sub-index j denotes the $j-th$ row of the linear operators $\mathcal{Z}^{k_h}, \mathcal{Z}^{k_t}$ (this notation will be used throughout the

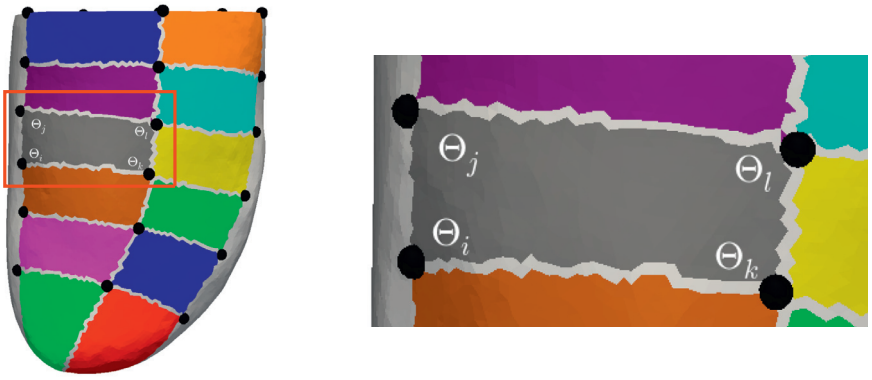

(a) Global view on patches and DOF (b) Close up at one specific patch

Fig. 2. Visualization of patches and respective DOF used for fiber angle discretization on a sample surface. Black spheres indicate the DOF locations, and the surface patches are separated by colors.

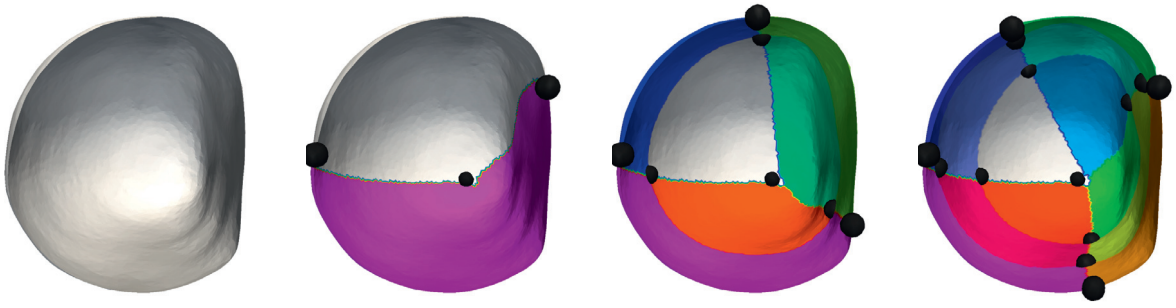

(a) k=1, $\kappa(k) = 2$ (b) k=2, $\kappa(k) = 6$ (c) k=3, $\kappa(k) = 14$ (d) k=4, $\kappa(k) = 26$

Fig. 3. Base to apex view on different patches resolution for the parametrizable angle models. Black spheres indicate the DOF locations, and the surface patches are separated by colors. Only the epicardial surface is shown for the sake of clarity, the split in the endocardial surface is analogous. Left side of the surfaces corresponds to the free wall, and right side to the septum.

manuscript). The matrices $\mathcal{Z}^k : \mathbb{R}^{\kappa(k)} \to \mathbb{R}^p$ correspond to linear harmonic lifting operators that first interpolate the angle DOF (e.g. $\boldsymbol{\Theta}$ or $\boldsymbol{\Phi}$) from the patches corners to the interior of the patches (and therefore to the whole ventricular surface), and then from the surface to the ventricular volume using a three-dimensional Poisson interpolation, see scheme in Fig. 4. A detailed explanation on how $\mathcal{Z}^k$ and also the local vectors $\boldsymbol{c}$, $\boldsymbol{\ell}$, $\boldsymbol{n}$ are computed can be found in Nagler et al. (2016).

The function $\tau(\beta, t(\boldsymbol{x}_j))$ models the nonlinear variation of the helix angle through the wall by

$$\tau(\beta, t(\boldsymbol{x})) = 1 + \beta\big(t(\boldsymbol{x}) - t(\boldsymbol{x})^2\big), \tag{5}$$

where the scalar $t \in [0, 1]$ represents the *transmural* coordinate (0 for epi- and 1 for endocardium). The parameter β is an additional DOF to be estimated from the data, and we restrict it to $\beta > -4$ to ensure that $\tau > 0$. The multiplicative approach (4) together with $\tau(\beta, \{0, 1\}) = 1 \ \forall \ \beta$ assures that DOF and helix angle values match on the heart's surface. Reported evidence show that a transmural nonlinearity of the helix angle can have a cubic-like shape (Streeter and Bassett, 1966) or a tanh-like shape (Ennis et al., 2008). The chosen form (5), after the linear transmural interpolation created by $\mathcal{Z}^{k_h}$, can reasonably approach these cases.

We point out that the resulting interpolated angle field is continuous in the whole left ventricle domain Ω due to the construction of $\mathcal{Z}^k$, which is strongly supported by histological studies of cardiac muscle (Streeter et al., 1969; Fernandez-Teran and Hurle, 1982).

The number of DOF for each angle type is given by $\kappa(k) = 2(k(k-1)+1)$, with the index k referring to the patch having k DOF in both axial and circumferential directions, see Fig. 3 for examples. The formula for $\kappa(k)$ arises from the fact that there is one continuous endo- and one epicardial surface and the degrees of freedom at the apex are merged to one. The resolution k of the patches will be chosen automatically depending on the available data, as it is explained in the next section.

2.3. Data-dependent parameter selection in estimation problems

In the later methodological steps we use a maximum likelihood approach in order to estimate the DOF of the fiber model, together with the diffusivities of the diffusion DT. Denoting all parameters to be estimated as $\boldsymbol{\alpha} \in \mathbb{R}^{\kappa\boldsymbol{\alpha}}$, this approach is based on maximizing the probability that the model (depending on the parameters) reproduces the measurements $\boldsymbol{G} \in \mathbb{R}^N$. In numerical practice, the probability $p(\boldsymbol{G}|\boldsymbol{\alpha})$ is not directly maximized, but actually $-\ln p(\boldsymbol{G}|\boldsymbol{\alpha}) =: J(\boldsymbol{\alpha})$ is minimized, namely the maximum likelihood estimate $\widehat{\boldsymbol{\alpha}}$ corresponds to

$$\widehat{\boldsymbol{\alpha}} = \underset{\boldsymbol{\alpha}}{\operatorname{argmin}} J(\boldsymbol{\alpha}) \tag{6}$$

For instance, by assuming an additive Gaussian noise in the measurements, $J(\boldsymbol{\alpha})$ leads to the classical least squares formulation.

As in every inverse problem, the estimation results are sensitive to the number of parameters chosen and to the amount of data available. A low number of parameters will lead to underfit-

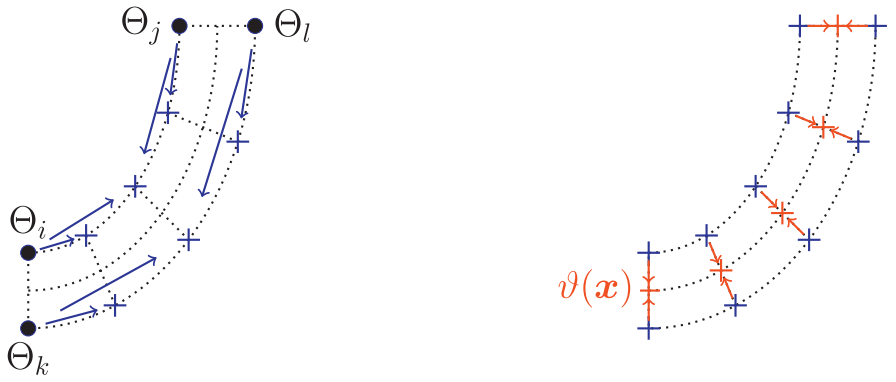

(a) Interpolation of DOF (black spheres) to surface nodes (blue crosses)

(b) Poisson interpolation of surface node values (blue crosses) into the domain nodes (red crosses).

Fig. 4. Sketch of linear operator $\mathcal{Z}^k$, which is composed in two steps.

ting while a "high" number will overfit the model, decreasing the estimation accuracy, in particular in the presence of noise. Conveniently, in the absence of a ground truth the maximum likelihood estimation framework gives quantitative tools to choose the resolution of the parameter space, depending on the available data. The most classical approach is the *corrected Akaike Information Criteria* (AICc):

$$\mathrm{AICc}(\widehat{\boldsymbol{\alpha}}) = 2J(\widehat{\boldsymbol{\alpha}}) + 2\kappa_{\boldsymbol{\alpha}} \frac{N}{N - (\kappa_{\boldsymbol{\alpha}} + 1)} \tag{7}$$

Therefore, while increasing the number of parameters will reduce the value of $J(\widehat{\boldsymbol{\alpha}})$, the second term penalizes this increase, trading-off the goodness of fit and model complexity. For a given set of maximum likelihood estimates $\widehat{\boldsymbol{\alpha}_1}, \widehat{\boldsymbol{\alpha}_2}, \ldots, \widehat{\boldsymbol{\alpha}_\Pi}$ with dimensions $\kappa_{\boldsymbol{\alpha}_1}, \kappa_{\boldsymbol{\alpha}_2}, \ldots, \kappa_{\boldsymbol{\alpha}_\Pi}$, respectively, the optimal parameter set $\widehat{\boldsymbol{\alpha}}_{\overline{k}}$ should be selected such that the AICc values are minimal, i.e.

$$\overline{k} = \underset{k=1,\ldots,\Pi}{\operatorname{argmin}} \mathrm{AICc}(\widehat{\boldsymbol{\alpha}_k}) \tag{8}$$

The derivation of AICc can be found in the original references (Akaike, 1974; Hurvich and Tsai, 1989). We further refer e.g. to Burnham and Anderson (2004) for an introduction of information criteria.

2.4. The maximum likelihood fiber estimator (MLFE)

In this section, we will detail the different steps of the MLFE, consisting of:

- Steps 1–2: Setup of the interpolation operators from the values at the patches corners into the image voxel centers.
- Steps 3–4: Reconstruction of the non-diffusion weighted data for the three-dimensional computational mesh. The reconstruction is based on a linear least squares approach which estimates values of the non-weighted information at the patches corners from the multislice non-weighted data.
- Steps 5–8: Formulation and solution of the non-linear optimization problems for fiber angle estimation using the diffusion weighted data. This includes an initial optimization run to identify the necessary restriction. Furthermore the final choice of the patches resolution based on Akaike's criteria.

We assume that we have $N^{(i)} \in \mathbb{N}$ voxels of measured diffusion weighted gray values $g_1^{(i)}, \ldots, g_{N^{(i)}}^{(i)}$ for each diffusion encoding direction $\boldsymbol{b}^{(i)}$, $i = 0, \ldots, N_{\mathrm{grad}}$, with $\boldsymbol{b}^{(0)} = \boldsymbol{0}$. To reduce the drawbacks

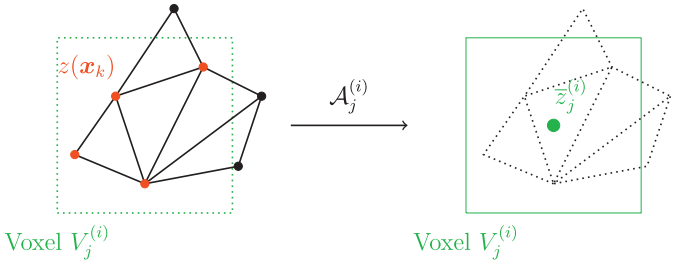

Fig. 5. Schematic illustration of operator $\mathcal{A}_j^{(i)}$. The black polygon represents the tetrahedral mesh, where the circles indicate the corresponding vertices lying within (red) or outside (black) the voxel. The scalar quantities on the nodes and those interpolated to the voxel center are represented with $z(\boldsymbol{x}_k)$ and $\bar{z}_j^{(i)}$, respectively. (For interpretation of the references to colour in this figure legend, the reader is referred to the web version of this article.)

of partial volume effects and ambiguities of endocardial trabeculations, like the papillary muscles, we consider only voxels with center lying inside the computational domain Ω. The MLFE consists of the following steps:

Step 1: Compute the operators mapping the DOF values to the ventricular domain, i.e. $\mathcal{Z}^k : \mathbb{R}^{\kappa(k)} \to \mathbb{R}^p$, for each patch refinement level $k = 1, \ldots, \Pi$, with Π a preset maximum number of patch refinements. A schematic illustration of the linear operator is given in Fig. 4 and examples of different patch refinements are illustrated in Fig. 3.

Step 2: Compute the linear interpolation mappings $\mathcal{A}^{(i)} : \mathbb{R}^p \to \mathbb{R}^{N^{(i)}}$, $i = 0, \ldots, N_{\mathrm{grad}}$ between the nodes of the mesh domain $\boldsymbol{x}_1, \ldots, \boldsymbol{x}_p$ and the $N^{(i)}$ voxels of the i-th DWI. An exemplary schematic representation of operator $\mathcal{A}_j^{(i)}$ is given in Fig. 5.

Step 3: Compute a reconstruction $\boldsymbol{\gamma}^0 \in \mathbb{R}^p$ in the whole domain Ω from the given non-diffusion weighted gray values $g_1^{(0)}, \ldots, g_{N^{(0)}}^{(0)}$ through the following maximum likelihood estimation problems:
For each patch refinement level $k = 1, \ldots, \Pi$, solve

$$\left\{\hat{\boldsymbol{z}}^k, \hat{\varsigma}\right\} = \underset{\boldsymbol{z},\, \varsigma}{\operatorname{argmin}} J_k^0(\boldsymbol{z}, \varsigma)$$
$$= \underset{\boldsymbol{z},\, \varsigma}{\operatorname{argmin}} \left(\frac{N^{(0)}}{2} \log 2\pi\varsigma^2 + \frac{1}{2\varsigma^2} \sum_{j=1}^{N^{(0)}} \left(g_j^{(0)} - \mathcal{H}_j^k \boldsymbol{z}\right)^2 \right) \tag{9}$$

$$\text{s.t.}\quad \left(\mathcal{V}^k\right)^\intercal \boldsymbol{z} - \left(\mathcal{V}^k\right)^\intercal \boldsymbol{I}_k(\hat{\boldsymbol{z}}^{k-1}) = 0,\ \ , k > 1, \tag{10}$$

where $\boldsymbol{z}$ represents the non-diffusion weighted values at the patch corners (to be estimated from the multi-slice data) and ς is the standard deviation of non-diffusion weighted grayvalues. The matrix $\mathcal{H}_j^k = \mathcal{A}_j^{(0)}\mathcal{Z}^k$ summarizes the DOF-to-voxel interpolation, while $\mathcal{V}^k$ corresponds to the matrix of eigenvectors of the Hessian $\left(\mathcal{H}^k\right)^\intercal\mathcal{H}^k$ for the smallest eigenvalues under a given threshold λ^0_{thres}, as proposed e.g. by Lieberman et al. (2013). Additionally $\boldsymbol{I}_k(\hat{\boldsymbol{z}}^{k-1})$ is the evaluation of the lower DOF-level estimate $\hat{\boldsymbol{z}}^{k-1}$ interpolated to the k-th (finer) patch vertices. This approach is an elegant way for reconstructing the model parameters which are hard to identify from the data due to the chosen patch refinement level but can be extrapolated from estimations on coarser patch levels. We will discuss the choice of λ^0_{thres} (constant among all k) in Section 2.5. Finally, choose the estimation on patch k satisfying the minimal AICc

$$\hat{k} = \underset{k}{\operatorname{argmin}}\,\mathrm{AICc}_k = \underset{k}{\operatorname{argmin}}\, 2\,J_k^0(\hat{\boldsymbol{z}}^k, \hat{\varsigma}) + 2\,d\,\frac{N}{N-d-1},$$

with $d = \kappa(k)+1$ the total number of DOF, and reconstruct the non-diffusion weighted values on the whole heart domain by $\boldsymbol{\gamma}^0 = \mathcal{Z}^{\hat{k}}\hat{\boldsymbol{z}}^{\hat{k}}$.

Step 4: Compute the scalar signal attenuation $\gamma_{i,j} \in \mathbb{R}$ for every voxel $j = 1,\dots,N^{(i)}$ of every diffusion encoding direction $i = 1,\dots,N_{\text{grad}}$ via

$$\gamma_{i,j} = \frac{g_j^{(i)}}{(\mathcal{A}_j^{(i)}\boldsymbol{\gamma}^0)}. \tag{11}$$

Step 5: Formulate the following optimization problem for every combination of patches resolution for the helix and transverse angles $k_h, k_t = 1,\dots,\Pi$. We assume that the diffusion-weighed measurements are independently normally distributed, i.e. $\gamma_{i,j} \sim \mathcal{N}(\mu_{i,j}, \sigma^2)$, where $\mu_{i,j}$ the mean value for the signal attenuation and σ the respective standard deviation. The expectation is modeled using Eq. (1) with the diffusion tensor given by (2). Combining it with the fiber angle parametrization (4), the parametrized signal attenuation is described as:

$$\mu_{i,j}(\boldsymbol{\Theta},\boldsymbol{\Phi},\beta,\boldsymbol{\lambda}) = \exp\left(-\boldsymbol{b}_i^\intercal\mathcal{D}\left(\vartheta(\boldsymbol{\Theta},\beta),\varphi(\boldsymbol{\Phi}),\boldsymbol{\lambda},\bar{\boldsymbol{c}},\bar{\boldsymbol{\ell}}\right)\boldsymbol{b}_i\right) \tag{12}$$

$$= \exp\left(-\boldsymbol{b}_i^\intercal\mathcal{D}\left(\mathcal{A}_j^{(i)}\mathcal{T}(\beta)\mathcal{Z}^{k_h}\boldsymbol{\Theta}, \mathcal{A}_j^{(i)}\mathcal{Z}^{k_t}\boldsymbol{\Phi},\boldsymbol{\lambda},\bar{\boldsymbol{c}},\bar{\boldsymbol{\ell}}\right)\boldsymbol{b}_i\right). \tag{13}$$

where $\mathcal{T}(\beta) = \mathrm{diag}([\tau(\beta,t(\boldsymbol{x}_1))\dots\tau(\beta,t(\boldsymbol{x}_p))])$, and $\bar{\boldsymbol{c}},\bar{\boldsymbol{\ell}}$ the re-orthogonalization of $[\boldsymbol{c}(\boldsymbol{x}_1)\dots\boldsymbol{c}(\boldsymbol{x}_p)](\mathcal{A}_j^{(i)})^\intercal$ and $[\boldsymbol{\ell}(\boldsymbol{x}_1)\dots\boldsymbol{\ell}(\boldsymbol{x}_p)](\mathcal{A}_j^{(i)})^\intercal$.

Hence, we write the maximum likelihood estimate $\widehat{\boldsymbol{\alpha}}_{k_h,k_t} = [\ \hat{\boldsymbol{\Theta}},\hat{\boldsymbol{\Phi}},\hat{\beta},\hat{\boldsymbol{\lambda}},\hat{\sigma}\ ] \in \mathbb{R}^{\kappa_{\boldsymbol{\alpha}}}, \kappa_{\boldsymbol{\alpha}} = \kappa_h + \kappa_t + 4$ as the solution of the following non-linear minimization problem

$$\widehat{\boldsymbol{\alpha}}_{k_h,k_t} = \underset{\boldsymbol{\alpha}}{\operatorname{argmin}} J_{k_h,k_t}(\boldsymbol{\alpha}) \tag{14}$$

$$= \underset{\boldsymbol{\alpha}}{\operatorname{argmin}}\left(\frac{N}{2}\log 2\pi\sigma^2 + \frac{1}{2\sigma^2}\sum_{i=1}^{N_{\text{grad}}}\sum_{j=1}^{N^{(i)}}\left[\gamma_{i,j} - \mu_{i,j}(\boldsymbol{\Theta},\boldsymbol{\Phi},\beta,\boldsymbol{\lambda})\right]^2\cdot\chi_{i,j}\right) \tag{15}$$

with the indicator function $\chi_{i,j}$ for selecting the measurements satisfying $\gamma_{i,j} \in [0,1]$, which the model (1) is capable to reproduce. The integer resulting from $N = \sum_{i=1}^{N_{\text{grad}}}\sum_{j=1}^{N^{(i)}}\chi_{i,j}$ corresponds to the global count of voxels.

We also add to the minimization the following bounds for the parameters

$$|\boldsymbol{\Theta}_i| < 90^\circ,\ \ i = 1,\dots,\kappa_h \tag{16}$$

$$|\boldsymbol{\Phi}_i| < \varphi_{max},\ \ i = 1,\dots,\kappa_t \tag{17}$$

$$-\lambda_1, -\lambda_2, -\sigma < 0 \tag{18}$$

$$-\beta < 4. \tag{19}$$

where the reasoning and choice of bound $\varphi_{\max}$ is detailed below.

Step 6: Solve the whole optimization problem formulated in Step 5 for $k_h = k_t = \bar{k} = 1,\dots,\Pi$, with an initial condition $\boldsymbol{\alpha}_0 = \widehat{\boldsymbol{\alpha}}_{\bar{k}-1,\bar{k}-1}$ at each $\bar{k}$-th level. Then compute the eigenvalues of the Hessian of $J_{\bar{k},\bar{k}}(\boldsymbol{\alpha} = \widehat{\boldsymbol{\alpha}}_{\bar{k},\bar{k}})$, and evaluate a threshold λ_{thres} as explained in Section 2.5.

Step 7: For all patches $k_h, k_t = 1,\dots,\Pi$, solve the whole optimization problem formulated in Step 5, but including the linear equality constraint

$$\left(\mathcal{V}^{k_h,k_t}\right)^\intercal(\boldsymbol{\alpha} - \boldsymbol{\alpha}_0) = 0, \tag{20}$$

with $\mathcal{V}^{k_h,k_t}$ eigenvectors of the Hessian of $J_{k_h,k_t}(\boldsymbol{\alpha} = \boldsymbol{\alpha}_0)$, selected as indicated in Section 2.5, and the starting value set as

$$\boldsymbol{\alpha}_0 = \boldsymbol{I}_{k_h,k_t}(\widehat{\boldsymbol{\alpha}}_{k_h-1,k_t}, \widehat{\boldsymbol{\alpha}}_{k_h,k_t-1}), \tag{21}$$

with $\boldsymbol{I}_{k_h,k_t}(.)$ the extension of the similar operator defined in Step 3, but applied to all parameters contained in $\boldsymbol{\alpha}$, see Appendix A for a detailed description.

Step 8: Finally, choose the set of parameters $\widehat{\boldsymbol{\alpha}}_{k_h,k_t}$ (computed in Step 7) satisfying the minimal AICc

$$\{\hat{k}_h,\hat{k}_t\} = \underset{k_h,k_t}{\operatorname{argmin}}\,\mathrm{AICc}_{k_h,k_t} = \underset{k_h,k_t}{\operatorname{argmin}}\, 2J_{k_h,k_t}(\widehat{\boldsymbol{\alpha}}_{k_h,k_t}) + 2\kappa_\alpha\frac{N}{N-\kappa_\alpha-1}$$

and reconstruct the fiber angle field on the whole heart domain by $\hat{\vartheta}(\boldsymbol{x}_j) = \tau(\hat{\beta}, t(\boldsymbol{x}_j))\mathcal{Z}_j^{\hat{k}_t}\hat{\boldsymbol{\Theta}}$ and $\hat{\varphi}(\boldsymbol{x}_j) = \mathcal{Z}_j^{\hat{k}_t}\hat{\boldsymbol{\Phi}}$. The maximum-likelihood fiber estimator (MLFE) is then given by evaluating $\boldsymbol{f}(\hat{\vartheta},\hat{\varphi},\boldsymbol{c},\boldsymbol{\ell})$ using Eq. (3).

Remark 1. As it can be appreciated in Eq. (15), the maximum likelihood formulation of the estimation problem does not depend at all on the particular choice of the parametrization of the angles. In other words, it only sees a finite number of parameters to be optimized, independent to which basis functions these are associated to. Only in the notation of the optimization in Step 3, namely Eq. (9), it is assumed that the interpolators are linear with respect to the degrees of freedom. This can be however generalized to basis functions with nonlinear dependence of the parameters. Therefore, any spatial parametrization can be used in the framework with minor modifications.

Remark 2. The only truly user-dependent parameter in the algorithm is $\varphi_{\max}$, which we choose in the examples below as $\varphi_{\max} = 20^\circ$, which is consistent with the histological observations of Streeter (1979) and the values estimated from ex-vivo data sets (Lombaert et al., 2012). Numerically, we have observed that a bound for the transverse angle is required when some inconsistencies e.g. in the registration of the DWIs are present.

The maximal number of patches Π has to be chosen large enough to achieve an AICc minimum, while the values for $\lambda^0_{thres}, \lambda_{thres}$ are selected depending on the number of acquired image slices as it will be explained in Section 2.5.

2.5. Computation of the regularization thresholds

From a certain patch refinement level k, degrees-of-freedom appear that may not influence the reproduction of the diffusion measurements. Therefore, these parameters are hard to identify, but they are still required for the full three-dimensional reconstruction of the fiber angle field across the whole ventricular domain.

As an example, for N_{slices} short axis DWIs only the same amount of DOF in axial direction can be uniquely estimated. However, real DWIs are not perfectly aligned along the long-axis of the ventricle, and respiratory motion leads to a spread of slice positions across the ventricular geometry. Hence, it is very difficult to determine a priori the structure of DOF that may be optimal. Moreover, the noise in the data may make the choice of DOF in axial direction less than N_{slices} more reliable.

In spite of this issues, we require the MLFE to reasonably reconstruct fibers in regions, where DWIs are not available from measurements, but still using the ventricle-specific data only, without any prior information.

As it was already introduced in the different steps in Section 2.4, we proceed by taking advantage of the maximum likelihood formulation itself in order to tackle this issue. Concretely, when solving the minimization problems in Section 2.4, badly posed search directions appear, represented by small eigenvalues of the Hessian matrix (remember that the search directions in classical optimization algorithms are proportional to the inverse of the Hessian). Therefore, restricting the solution along these directions allows to deliver stable results. Doing so, not only the geometrical information – spatial location DOF versus DWIs positions – but also the sensitivity to the diffusion information – fiber versus gradient encoding directions – are automatically considered.

We recall that in Steps 3 and 7 search directions corresponding to eigenvalues of the Hessian smaller than certain thresholds λ^0_{thres} and λ_{thres}, respectively, are filtered out from the optimization. Since in our experience unrealistic fiber angle oscillations start to be noticeable at patch level $k = N_{\text{slices}}$ for the unrestricted case, we define the thresholds as follows:

- λ^0_{thres}= Smallest eigenvalue of the Hessian in Step 3 at patch $k = N_{\text{slices}} - 1$.
- λ_{thres}= Smallest eigenvalue of the Hessian in Step 5 at patch $\bar{k} = N_{\text{slices}} - 1$, evaluated at the optimal solution at patch $\bar{k} - 1$. Note that we exclude from the linear constraints (20) all eigenvectors, whose maximal component corresponds to the spatially constant parameters $(\sigma, \boldsymbol{\lambda}, \beta)$.

In Section 3.4, the sensitivity of the results to these thresholds will be illustrated, justifying the aforementioned choice.

Note that in Steps 3 and 7 the restricted search directions are fixed using the estimation of coarser patch refinements. This approach makes the whole MLFE algorithm purely data-driven without any need of a priori assumptions for the model parameters.

2.6. Numerical optimization

To solve the minimization problem (14)–(20) we use a subspace trust-region interior reflective algorithm (Branch et al., 1999; Byrd et al., 1988), where the constraints are included via barrier methods (Byrd et al., 1999; 2000; Waltz et al., 2006). The algorithm is implemented within the `Matlab` optimization toolbox (MATLAB, 2013), which takes into account the linear parameter constraints (16)-(20) directly using Lagrange multipliers. Since the diffusion tensor model has an analytical form with respect to the parameters to be estimated, we directly compute the gradient and Hessian matrix of the cost function and use them during the minimization procedure.

The numerical optimization scheme stops if the step size of the update or the change in the resulting cost function value, and all inequality conditions, are fulfilled with precision 10^{-14}. To assure the optimum was found, a second run was performed using the result of the first optimization as starting value.

3. Numerical examples with synthetic data

In this section, we introduce a numerical example based on synthetic data. The purpose is to analyze the performance of the MLFE in terms of a ground truth fiber field, and to compare its accuracy with the state of the art method, the curvilinear tensor interpolation (CLTI) of Toussaint et al. (2013). The CLTI is the only algorithm in the literature reported to reconstruct multi-slice DW-MRI from a specific individual only, without using fibers estimated from template diffusion data.

3.1. Reference fiber field

We generated two reference fiber families on a prolate spheroid geometry named *smooth* and *perturbed*, see Fig. 6. The details of the construction of the reference geometry are given in Appendix B. The perturbed fiber field is motivated from studies reporting local changes in the myocardial fiber architecture after infarction (Chen et al., 2003).

Both fiber families are constructed first on the original analytical spheroid geometry using formula (3) with zero transverse angle, i.e. $\boldsymbol{f}(\theta(\mu, \nu, \phi), 0, \boldsymbol{g}_1, \boldsymbol{g}_2)$. The local coordinate system is defined by the derivatives of the prolate spheroid coordinates $\boldsymbol{g}_1 = d\boldsymbol{x}/d\phi$ and $\boldsymbol{g}_2 = -d\boldsymbol{x}/d\nu$ (see Equations (B.1)-(B.3) in Appendix), succeeded by a re-orthonormalization. The smooth and perturbed fiber families are defined by changing the helix angle only, namely by $\theta_{\text{smooth}}(\mu, \nu)$ and $\theta_{\text{perturbed}}(\mu, \nu, \phi) = \theta_{\text{smooth}}(\mu, \nu)h(\phi, \nu, \mu)$, respectively. These are given precisely as:

- Quadratic variation of the helix angle in long-axis direction z from -40° to -60° (epicardium) and 48° to 72° (endocardium):

$$\theta_{\text{smooth}}(\mu, \nu) = \underbrace{\frac{\tanh(\alpha(2\tilde{\mu} - 1))}{\tanh(\alpha)}}_{\text{nonlinear transmural variation}} \times \underbrace{\left(-60^\circ + 20^\circ\left(\frac{z(\mu, \nu)}{z_{min}}\right)^2\right)}_{\text{apex-to base variation}} \underbrace{(1.2 - 0.2\tilde{\mu})}_{\text{offset for endocardium}} \tag{22}$$

  where $\tilde{\mu}(\mu) = \frac{\mu - \mu_1}{\mu_2 - \mu_1}$ the normalized in-wall coordinate, $z_{\min}$ the minimal z-component of the nodes in Ω and $\alpha = 1.5$.
- For the perturbed case a systematic shift on the helix angle respectively the circumferential direction ϕ (with 50% transmurality) was imposed via

$$h(\phi, \nu, \mu) = \begin{cases} 1 - \frac{1}{2}\sin(2\phi - 180^\circ) & \text{for } \{\phi, \nu, \mu\} \in [90^\circ, 180^\circ] \\ & \quad \times [108^\circ, 144^\circ] \times [\mu_1, \frac{\mu_1 + \mu_2}{2}] \\ 1 & \text{elsewise,} \end{cases} \tag{23}$$

  see more blue fibers in Fig. 6(c)-left.
- To create a more realistic left ventricular geometry, we applied a force on one side of the free wall within a quasi-static nonlinear structural simulation, which induces a geometrical asymmetry. The fiber directions were not modified. This additionally allows for including a non-zero transverse angle, see Fig. 6(a)-6(c) right. Notice also that this distortion allows to test the CLTI

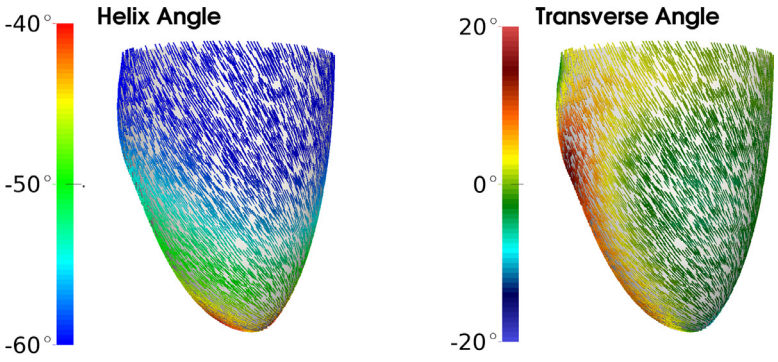

(a) Healthy & perturbed epicardial fibers

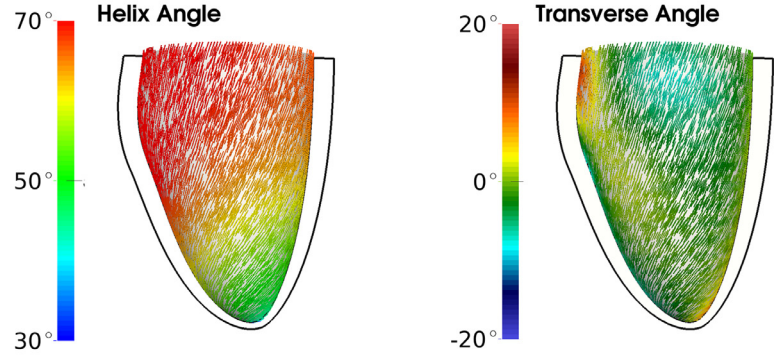

(b) Healthy endocardial fibers

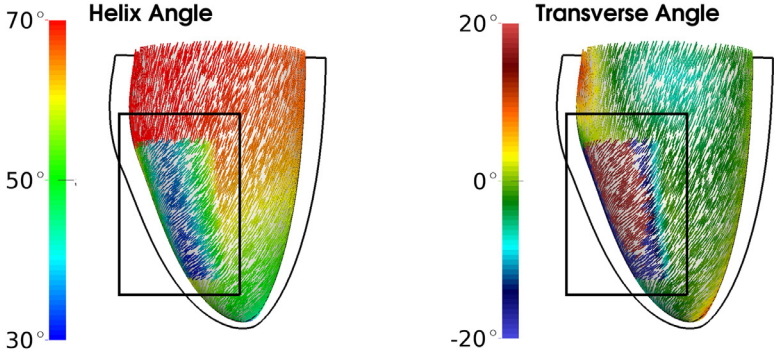

(c) Perturbed endocardial fibers

Fig. 6. Glyph plot of synthetic fiber organization, namely smooth and perturbed, at the epi- and endocardial surface colored according the fiber angle. Endocardial cases are supported by the cut view of the domain (black). Perturbed area (within the black box) at endocardium (c) is located in the area with more horizontal (blue) helix angles. (For interpretation of the references to colour in this figure legend, the reader is referred to the web version of this article.)

approach in a configuration, where its assumption about the geometry does not fully hold.

Remark 3. The rule based model used in this manuscript considers a "piecewise" linear and continuous variation of the angles in circumferential and long-axis directions. Hence, it cannot exactly reproduce the nonlinear spatial variation on the surface of the reference fiber. However, we will see later that this does not prevent from an excellent performance in the fiber reconstruction.

3.2. Synthetic DWIs

From the smooth and perturbed fiber families we construct DWIs for $N_g = 15$ diffusion encoding directions given in Table 1, which were chosen in order to uniformly cover the whole sphere at the usual resolution in real in-vivo acquisitions (Jones et al., 1999). We consider $N_{\text{slices}} = 5$ equally distributed along the long axis of the ventricle depicted in Fig. 7(a), similar to recent reports of 4 (Harmer et al., 2013) and 6 (Stoeck et al., 2014) slices in real in-vivo DW-MRI acquisitions.

At each of the slices, the voxel size is assumed to be $2 \times 2 \times 8\text{mm}^3$. At the center of each voxel, the fiber angles and local

Table 1
Gradient diffusion encoding directions.

$\boldsymbol{b}^{(0)}$	$\boldsymbol{b}^{(1)}$	$\boldsymbol{b}^{(2)}$	$\boldsymbol{b}^{(3)}$	$\boldsymbol{b}^{(4)}$	$\boldsymbol{b}^{(5)}$	$\boldsymbol{b}^{(6)}$	$\boldsymbol{b}^{(7)}$
$\begin{bmatrix}0\\0\\0\end{bmatrix}$	$\begin{bmatrix}1\\0\\0\end{bmatrix}$	$\begin{bmatrix}0\\1\\0\end{bmatrix}$	$\begin{bmatrix}0\\0\\1\end{bmatrix}$	$\begin{bmatrix}\frac{2}{\sqrt{5}}\\\frac{1}{\sqrt{5}}\\0\end{bmatrix}$	$\begin{bmatrix}-\frac{2}{\sqrt{5}}\\\frac{1}{\sqrt{5}}\\0\end{bmatrix}$	$\begin{bmatrix}\frac{1}{\sqrt{5}}\\\frac{2}{\sqrt{5}}\\0\end{bmatrix}$	$\begin{bmatrix}-\frac{1}{\sqrt{5}}\\\frac{2}{\sqrt{5}}\\0\end{bmatrix}$
$\boldsymbol{b}^{(8)}$	$\boldsymbol{b}^{(9)}$	$\boldsymbol{b}^{(10)}$	$\boldsymbol{b}^{(11)}$	$\boldsymbol{b}^{(12)}$	$\boldsymbol{b}^{(13)}$	$\boldsymbol{b}^{(14)}$	$\boldsymbol{b}^{(15)}$
$\begin{bmatrix}\frac{1}{\sqrt{2}}\\0\\\frac{1}{\sqrt{2}}\end{bmatrix}$	$\begin{bmatrix}\frac{1}{\sqrt{2}}\\0\\-\frac{1}{\sqrt{2}}\end{bmatrix}$	$\begin{bmatrix}0\\\frac{1}{\sqrt{2}}\\\frac{1}{\sqrt{2}}\end{bmatrix}$	$\begin{bmatrix}0\\\frac{1}{\sqrt{2}}\\-\frac{1}{\sqrt{2}}\end{bmatrix}$	$\begin{bmatrix}\frac{1}{\sqrt{3}}\\\frac{1}{\sqrt{3}}\\\frac{1}{\sqrt{3}}\end{bmatrix}$	$\begin{bmatrix}-\frac{1}{\sqrt{3}}\\\frac{1}{\sqrt{3}}\\\frac{1}{\sqrt{3}}\end{bmatrix}$	$\begin{bmatrix}-\frac{1}{\sqrt{3}}\\\frac{1}{\sqrt{3}}\\-\frac{1}{\sqrt{3}}\end{bmatrix}$	$\begin{bmatrix}\frac{1}{\sqrt{3}}\\\frac{1}{\sqrt{3}}\\-\frac{1}{\sqrt{3}}\end{bmatrix}$

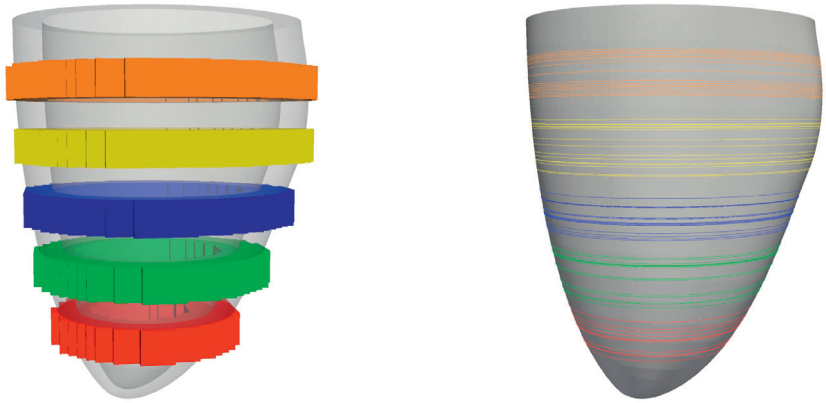

(a) Original

(b) After added displacement and registration ($\sigma_\delta = 7.5$mm)

Fig. 7. Measurement slices positions. (a) Target positions (i.e. with out motion distortions), showing the voxel thickness. (b) Mid plane of all DWI slices including motion distortions, intersected with 3D geometry.

orthonormal system $\boldsymbol{c}$, $\boldsymbol{\ell}$ were computed using the operator $\mathcal{A}^{(i)}$, and followed by the evaluation of reference diffusion tensor $\mathcal{D}_{\text{ref}}$ from (2)–(3), with constant diffusivities as $\lambda_1 = 0.8$ and $\lambda_2 = 0.5$ (diffusivities scaled by the constant b-value) for both smooth and perturbed cases. At each voxel $V_j^{(i)}$, $j = 1, \ldots, N^{(i)}$, we compute the signal intensity $g_j^{(i)}$ for each gradient direction $\boldsymbol{b}^{(i)}$ via:

$$g_j^{(i)} = g_j^{(0)} \exp(-\boldsymbol{b}^{(i)\mathsf{T}} \mathcal{D}_{\text{ref}} \boldsymbol{b}^{(i)}) \tag{24}$$

with the uniform unweighted intensity $g_j^{(0)} = 100$.

The measurements were then perturbed as follows:

Spatial mismatch. To include the inevitable spatial mismatch of the in-vivo acquired DWIs for each slice caused by breathing, we model respiration-induced motion by applying a rigid body translation to the computational mesh Ω of amplitude $\delta_{i,k}$ and diaphragm motion direction $\boldsymbol{d}$, with $\delta_{i,k} \sim \mathcal{N}(0, \sigma_\delta^2)$ a random variable generated independently for every slice $k = 1, \ldots, 5$ and diffusion gradient direction $i = 0, \ldots, N_g$. Furthermore, we assume that this is the only motion related distortion, meaning that the images are acquired at a similar same moment of the cardiac cycle.

The direction $\boldsymbol{d}$ was considered to be in foot-to-head direction, what was assumed to be given by rotations of the ellipsoid long axis of 30^o and 15^o with respect to the y- and x-axis, respectively. We used different standard deviations $\sigma_\delta \in \{0.0, 2.5, 5.0, 7.5\}$mm. The value of 2.5mm is the most commonly reported acceptance window currently used in human in-vivo cardiac DW-MRI acquisitions (Nielles-Vallespin et al., 2013; Stoeck et al., 2014; 2015). Note also that the locations of the DWIs with respect to the global coordinate system are kept fixed, as it is done in real acquisitions.

Registration. Since the MLFE can handle non-matching DWIs, we can therefore register each DWI to the "true heart location" before running the estimation. The registration was performed by the open source software *elastix* (Klein et al., 2010) using binary masks of the moved DWIs and the original 3D ventricular geometry. The final position of the slices with respect to the heart's geometry are exemplified for $\sigma_\delta = 7.5$mm in Fig. 7(b). Note that this adds another source of imprecision to the data, as encountered in real acquisitions, since the registration procedure is not capable to find the exact positions of the DWI slices with respect to an independently acquired 3D morphology.

Notice that the final perturbation of the slices position with respect to the ventricular geometry include both axial and in-plane motion artifacts, see Fig. 7(b) and 8(b), respectively. Fig. 7(b) only shows schematically the intersections of the perturbed slices with the 3D ventricular geometry. In Fig. 8(b), the in-plane component of the perturbation can be clearly recognized.

Since we modify the slice position by the registration step, we simultaneously have to adapt the orientation of the diffusion encoding directions. But in fact, since we are currently using a rigid registration, nothing has to be adapted at all, this is a trivial step.

Noise. We also consider adding Rician noise to $g_j^{(i)}$ with a complex Gaussian deviation $\sigma_{\text{Gauss}} = 7$ in order to emulate a more realistic testing scenario (Gudbjartsson and Patz, 1995). The resulting signal-to-noise ratio (SNR) is about 14 for the non-diffusion weighted images and about 7 for the diffusion encoded images. The chosen SNR is within the range of reported values (von Deuster et al., 2015). Figs. 8(b) and 8(c) show the effects of the motion artifact and noise for a mid-ventricular slice, respectively.

Outliers. Due to imperfect registration of the DWIs with respect to the 3D ventricle, the measured DWIs may include few gray values from background voxels, which can deteriorate the estimation quality of $\boldsymbol{\gamma}^0$ and $\widehat{\boldsymbol{\alpha}}$. We will therefore utilize an outlier detection scheme as routinely used in estimation practice (Upton and Cook, 1996). For our problem, we will apply the well-known *interquartile distance* (IQD), so that all gray values lying outside the range (median $\pm$ 2 IQD) are neglected.

3.3. Comparison to curvilinear tensor interpolation method

The performance of the proposed MLFE is compared to the curvilinear tensor interpolation (CLTI), recently presented by Toussaint et al. (2013). We refer to Section 5.4 for a discussion concerning other reported approaches for cardiac fiber estimation.

In order to apply the CLTI to the numerical examples, we must proceed in the following way, since the CLTI relies on the spatial co-existence of the diffusion information. First, a mean image is computed from the DWIs belonging to the same acquired slice (same colors in Fig. 7(b)). Secondly, each DWI is registered in-plane to the mean image. Subsequently, the mean DWI is in-plane registered onto the 3D acquisition of the left ventricular (LV) geometry,

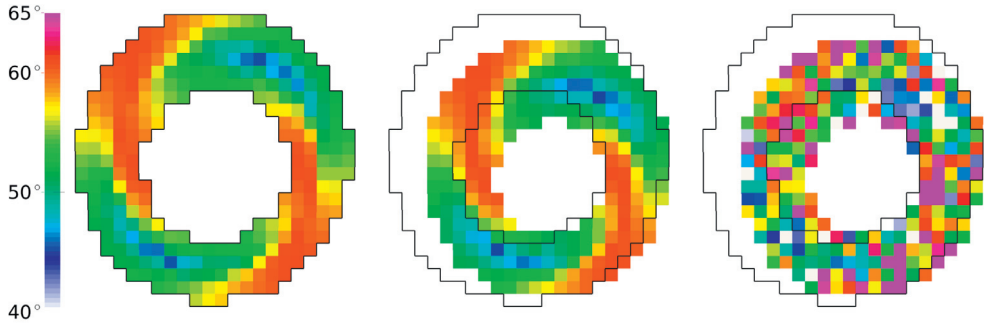

(a) $\sigma_\delta = 0.$, $\sigma_{\text{Gauss}} = 0$ (b) $\sigma_\delta = 7.5$, $\sigma_{\text{Gauss}} = 0$ (c) $\sigma_\delta = 7.5$, $\sigma_{\text{Gauss}} = 7$

Fig. 8. Example of an apical DWI (red slice in Fig. 7(a)), colored by gray value with (a) no noise, (b) motion perturbation and (c) motion perturbation and measurement noise. The black line represents the original slice position without motion perturbation. Note that only displacements in the in-plane direction of the short axis plane is observed, while the displacement in the long-axis direction is captured by the different diameters of the LV. (For interpretation of the references to colour in this figure legend, the reader is referred to the web version of this article.)

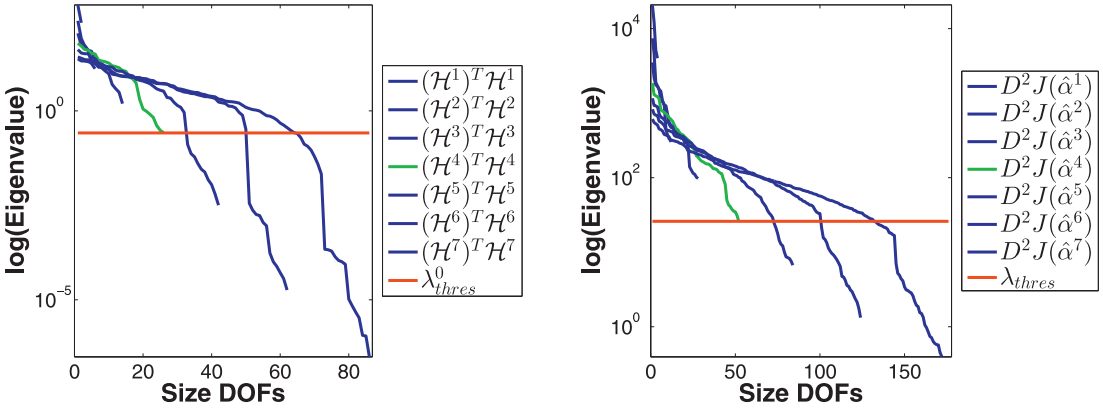

(a) Eigenvalues for the non-weighted diffusion data estimate (Step 3) (b) Eigenvalues for the MLFE (Step 6)

Fig. 9. Eigenvalue distribution against number of DOF in several patch refinement levels for the Hessian matrices of functional in Steps 5 in the smooth synthetic case using $\sigma_\delta = 7.5$mm for patches refinement levels $1, \ldots, 7$. Eigenvalue distribution used for threshold evaluation is highlighted with green. (For interpretation of the references to colour in this figure legend, the reader is referred to the web version of this article.)

and the same registration displacement field is applied to each individual DWI. At each image voxel of the registered DWI data the diffusion tensors are linearly estimated. Finally, the LV domain and the diffusion tensors were diffeomorphically mapped onto an ideal prolate spheroid, and the tensors are interpolated in spheroid coordinates using a log-Euclidian metric. The final tensor field is obtained after mapping back onto the original LV geometry by inversion of the diffeomorphic transformation. The fiber field and diffusivity values are obtained via principal component analysis of the resulting tensor field.

3.4. Estimation results

We present now the estimation results for both smooth and perturbed synthetic examples using the algorithm described in Section 2.4. The sequence of patches used in this examples are computed analogously to the ones shown in Fig. 3.

In Fig. 9, the eigenvalues computed in Steps 3 and 6 are visualized for the smooth data set with $\sigma_\delta = 7.5$mm and the respective regularization thresholds. Though the threshold value for the eigenvalues is set from a coarser patch, increasing the patches resolution increases the final number of DOFs, making the MLFE capable to capture more detailed fiber orientations without getting spurious fiber angle oscillations.

Consistently with the original data, the minimal AICc for the non-diffusion weighted data was obtained for the very first patch (i.e. one DOF per surface). Then, the AICc maps (Step 8) of the resulting maximum likelihood estimate for $k_h, k_t = 1, \ldots, \Pi = 9$ focusing on the data with perturbation $\sigma_\delta = 7.5$mm is shown in Fig. 10. Note that the AICc criterion suggests a fine patch resolution for the transverse angle in the smooth case, and it also suggests a finer patch resolution for the helix angle in the perturbed case. Both choices are consistent with the ground truth, i.e. with the jump of transverse angle in the deformed region, and the systematic shift of the helix angle in circumferential direction in the perturbed case.

Fig. 11 show histograms and global statistics for the angle error ϵ between the ground truth fibers and the estimated fibers for both MLFE and CLTI. It can be generally appreciated that MLFE is robust with respect to motion perturbation and registration imprecision of the slices and consistently more accurate than CLTI.

To give the reader an impression about the sensibility of the MLFE method regarding the grayvalue and motion noise, the results are recomputed by leaving out the measurement noise, i.e. $\sigma_{\text{Gauss}} = 0$. The global results respective total angle error ϵ, helix angle error ϵ_{Helix}, transvers angle error ϵ_{Trans}, diffusivities and gaussian noise are given in Table 2. As can be appreciated from these table, the motion distortion itself does not much effect the

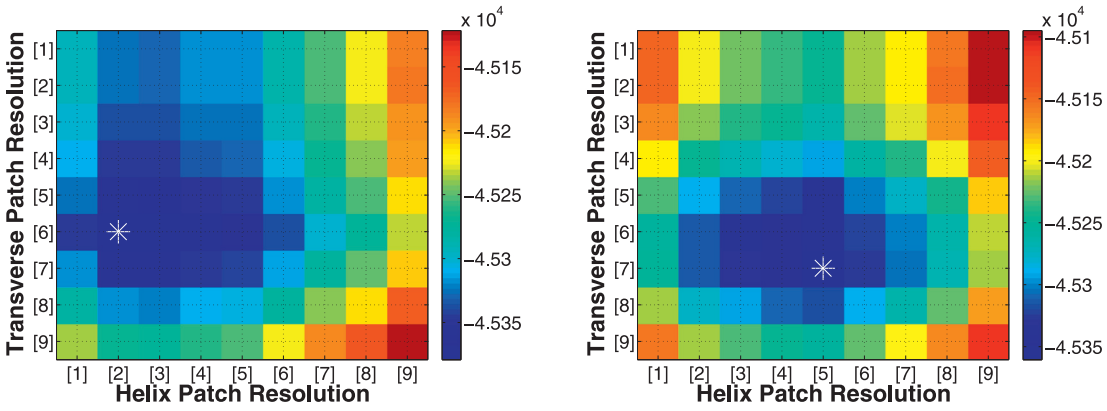

(a) AICc - smooth (b) AICc - perturbed

Fig. 10. AICc values plots (Step 8) for $\sigma_\delta = 7.5$mm. White star indicates the location of the minimum, and therefore that patch resolution was chosen for the results shown in the sequel and comparisons with CLTI.

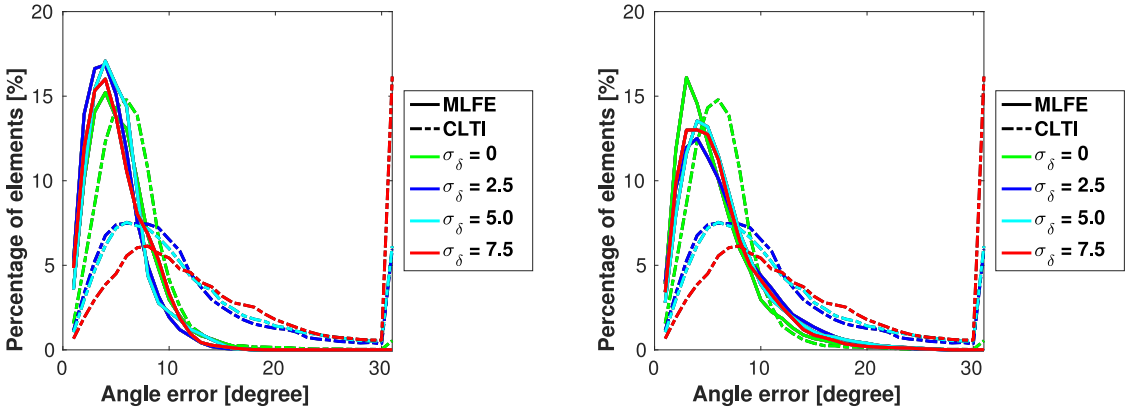

(a) Histogram for angle error: smooth case (b) Histogram for angle error: perturbed case

Method	σ_δ [mm]	mean(ϵ) ± std(ϵ) [°]
MLFE	0.0	4.78 ± 2.64
	2.5	5.32 ± 2.97
	5.0	5.92 ± 3.42
	7.5	5.47 ± 3.84
CLTI	0.0	6.11 ± 4.63
	2.5	11.31 ± 10.26
	5.0	11.88 ± 10.50
	7.5	18.10 ± 18.47

(c) Statistics for angle error: smooth case

Method	σ_δ [mm]	mean(ϵ) ± std(ϵ) [°]
MLFE	0.0	4.36 ± 2.90
	2.5	5.35 ± 3.07
	5.0	5.20 ± 3.22
	7.5	5.07 ± 2.99
CLTI	0.0	5.87 ± 4.93
	2.5	11.70 ± 9.67
	5.0	11.47 ± 10.24
	7.5	18.82 ± 19.89

(d) Statistics for angle error: perturbed case

Fig. 11. Global statistics of angle error between ground truth and estimated fiber orientation for MLFE and CLTI methods for both smooth and perturbed synthetic data sets and different motion perturbations.

reconstruction quality of the MLFE, since its effects are included in the model. The grayvalue noise instead does mainly increase the reconstruction error of the transverse angle.

The reconstruction quality of the MLFE and CLTI is further investigated by analyzing the accuracy of the results for each of 17 AHA regions (Cerqueira et al., 2002), see Fig. 12: when perturbing the slices positions, changes in the regional mean errors are around 2^o for non apical regions (AHA Region < 17), and around 5^o for the apex (AHA Region 17). In this figure it can also be appreciated that the large errors in the CLTI (i.e. the sharp increase after 30 degrees of error in Fig. 11) come mainly from the fibers in the apical region.

In Fig. 13, the estimated fiber organizations on the ventricular geometry are presented. While the MLFE shows a similar fiber organization for both levels of motion distortion, the CLTI results in an highly oscillating fiber organization at the basal and apical parts for higher motion distortion with transverse angles up to 90°, confirming the previous findings from Figs. 11 and 12. This can be explained due to the fact that the eigenvalue analysis of the CLTI reconstructed tensor results in a principal eigenvector (i.e. related to

Table 2
Summary of angle error between ground truth and estimated fiber orientation for the MLFE methods for both smooth and perturbed synthetic data sets using different noise and motion perturbations.

σ_δ	σ_{Gauss}	ϵ [°]	ϵ_{Helix} [°]	ϵ_{Trans} [°]	$\lambda_1 = 0.8$	$\lambda_2 = 0.5$	σ
smooth							
0.0mm	0	2.65 ± 2.07	1.78 ± 1.45	1.61 ± 1.87	0.800	0.500	2.57e-03
7.5mm	0	3.29 ± 2.32	2.55 ± 2.10	1.60 ± 1.68	0.798	0.501	6.42e-03
0.0mm	7	4.92 ± 2.85	2.83 ± 2.17	5.15 ± 3.79	0.781	0.496	0.068
7.5mm	7	4.61 ± 2.73	2.72 ± 2.11	6.19 ± 4.48	0.783	0.500	0.069
perturbed							
0.0mm	0	2.89 ± 2.47	2.08 ± 2.06	2.24 ± 3.63	0.800	0.500	2.57e-03
7.5mm	0	3.52 ± 2.65	2.79 ± 2.41	2.29 ± 3.75	0.798	0.501	6.4e-03
0.0mm	7	5.21 ± 3.78	3.16 ± 3.17	6.91 ± 5.31	0.789	0.500	0.068
7.5mm	7	5.66 ± 3.79	3.81 ± 3.45	6.33 ± 4.73	0.783	0.497	0.0685

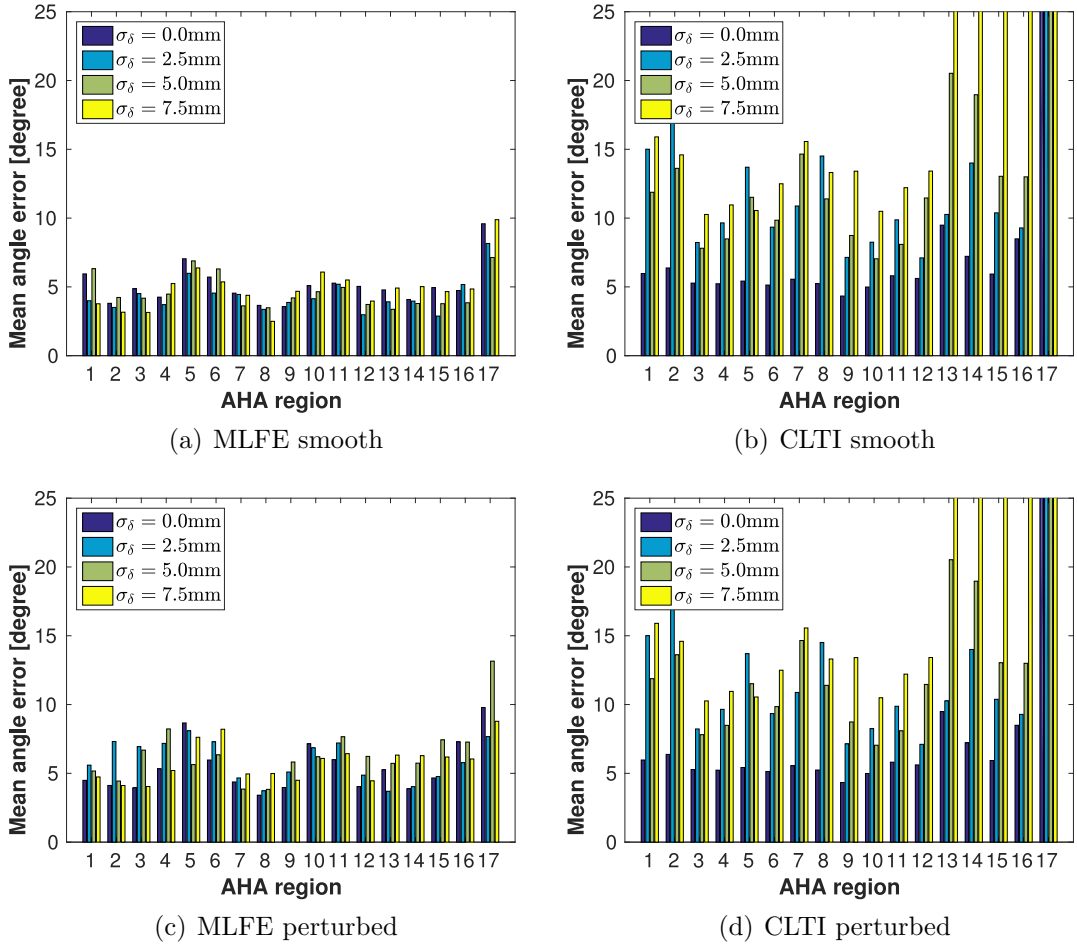

(a) MLFE smooth (b) CLTI smooth

(c) MLFE perturbed (d) CLTI perturbed

Fig. 12. Resulting mean fiber angle error between ground truth and estimated fiber orientation for MLFE and CLTI in each AHA region, for different motion artifacts.

the biggest eigenvalue), which does not refer to the fiber direction any longer. The only component of the MLFE that in our experience results in sensitive outputs is the choice of the regularization threshold, what we analyzed in Fig. 14. We show the result for $\mathcal{Z}^{k_h} = \mathcal{Z}^6$, $\mathcal{Z}^{k_t} = \mathcal{Z}^1$ using different eigenvalues for the regularization threshold. We appreciate that some spurious oscillations of the fiber orientation start at $\tilde{k} = N_{\text{slices}} = 5$, justifying the choice of the thresholds one refinement level before.

4. Fiber estimation from ex-vivo human DW-MRI

In this section, we present the results of the fiber angle estimation based on an ex-vivo human DW-MRI data set, which has been subsampled to meet typical in-vivo cardiac DW-MRI acquisition parameters, as done for the synthetic example. The goal is to assess the sensitivity of the MLFE and CLTI with respect to the motion of the DWIs, when dealing with real DW-MRI data.

4.1. Data and model setups

We obtained the diffusion weighted images (DWI) from the ex-vivo human DW-MRI data openly available from the John Hopkin's University database[1] and segment a surface representation of the left ventricular domain from the non-diffusion weighted MRI data, which has a spatial resolution of 0.43mm × 0.43mm × 1.0mm, using MIMICS (Materialise, Leuven, Belgium). In a next step we produced a tetrahedral computational mesh of about 110k nodes using `Gmsh` (Geuzaine and Remacle, 2009), see Fig. 15(a). Analogously

[1] http://www.ccbm.jhu.edu/research/dSets.php.

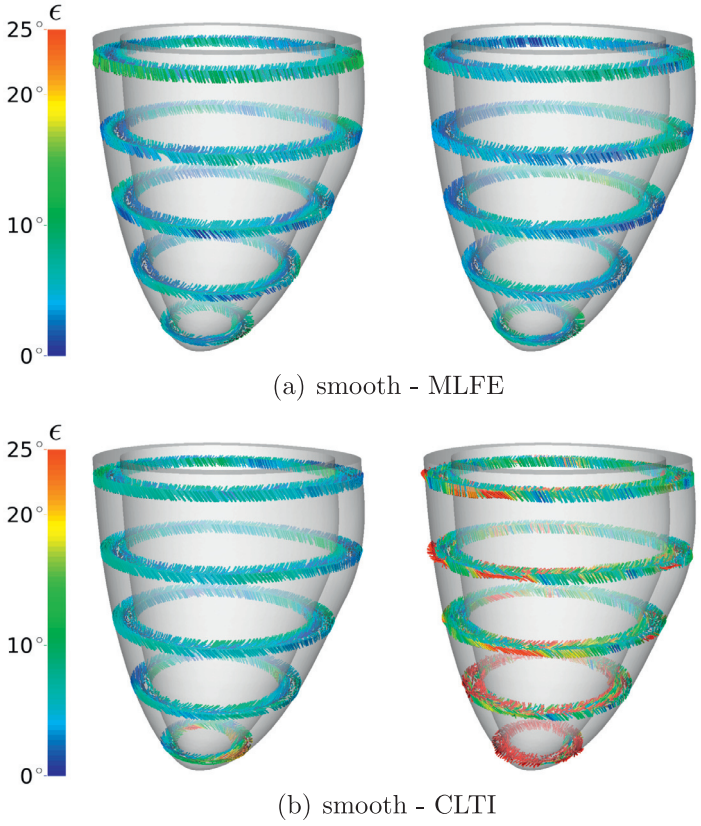

Fig. 13. Resulting fiber organization from MLFE and CLTI, colored according to angle error ϵ between ground truth and estimated fiber orientation, for motion distortion $\sigma_\delta = 0.0$ (left) and $\sigma_\delta = 7.5$ (right).

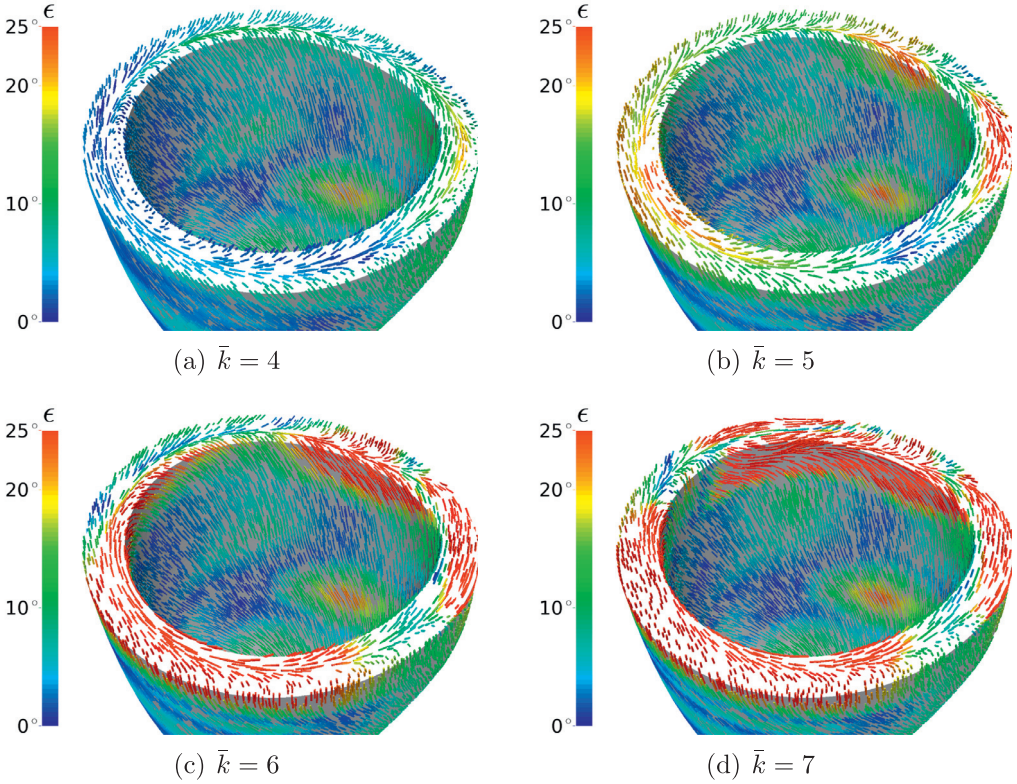

Fig. 14. Top view on resulting fiber organization of MLFE for Hessian eigenvalue thresholds chosen as smallest eigenvalue of different patches $\bar{k}$. Shown examples are from the smooth synthetic data sets with motion distortion $\sigma_\delta = 7.5$. Fibers are colored according to angle error ϵ between ground truth and estimated fiber orientation. Previous results in this section correspond to $\bar{k} = N_{\text{slices}} - 1 = 4$.

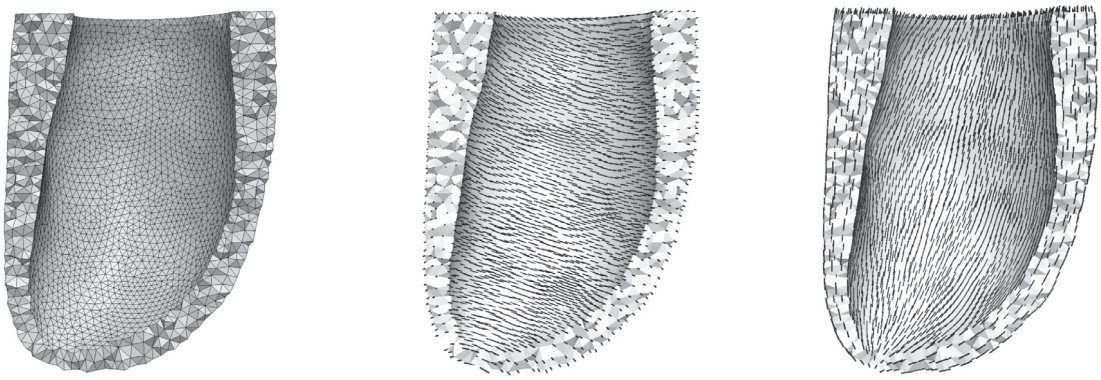

(a) Computational mesh (b) Local coordinate system

Fig. 15. Ventricular geometry for setup of the fiber model using a coarser mesh size for the sake of clarity. (a) Computational mesh and (b) local orthonormal coordinates in circumferential direction (left) and long axis direction (right).

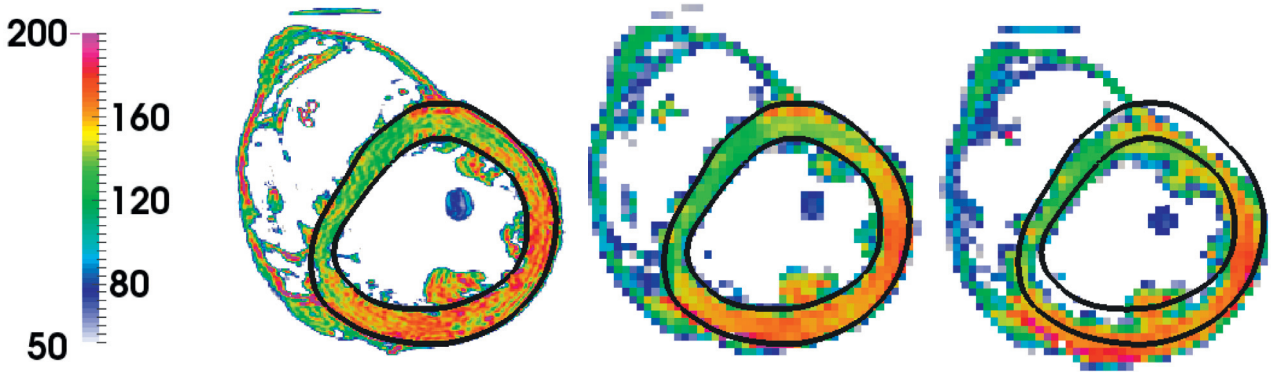

(a) Non diffusion weighted grayvalues $\boldsymbol{g}^{(0)}$

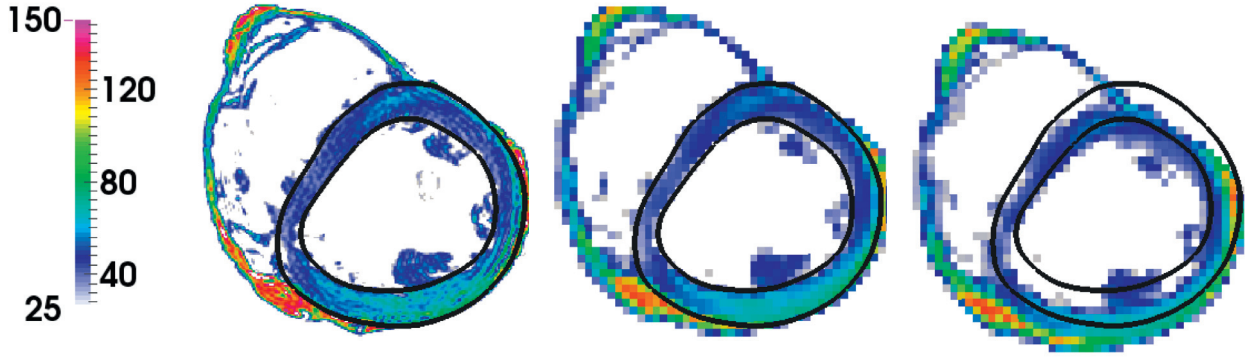

(b) Exemplary diffusion weighted grayvalues $\boldsymbol{g}^{(2)}$ using $\boldsymbol{b}^{(2)}$

Fig. 16. Exemplary grayvalue images for non-diffusion (top) and diffusion weighted (bottom) data at a midventricular position. Each figure shows the original (EV) data (left), downsampled data with no motion artifact (IVL, $\sigma_\delta = 0.0$mm) (middle) and downsampled data with respiratory motion of (IVL, $\sigma_\delta = 7.5$mm) (right, geometry and DWIs in the figure are not co-registered). For better comprehension of the motion distortion the contour of the 3D ventricular mesh (black line) is drawn.

to the distorted ellipsoid, we compute a local orthonormal coordinate system at every node of the computational mesh, visualized in Fig. 15(b).

4.2. Generation of measurements

Starting with the full information from the ex-vivo DWI data set (EV), i.e. 0.43mm × 0.43mm × 1.0mm voxel size for 20 diffusion encoding directions, we generated "in-vivo like" data (IVL) by considering 5 equidistant slices for each of the 20 DWIs of voxel size 2mm × 2mm × 8mm. The signal value was generated by averaging the signal intensities of the original voxels, which lie inside the downsampled voxel. We then perturbed the slices position as described in Section 3.2. The diaphragm motion direction $\boldsymbol{d}$ was chosen as $\boldsymbol{d} = [-0.2113, -0.8660, 0.4532]^\intercal$, where the heart's long axis is $[0, 0, 1]^\intercal$. We consider two measurement scenarios,

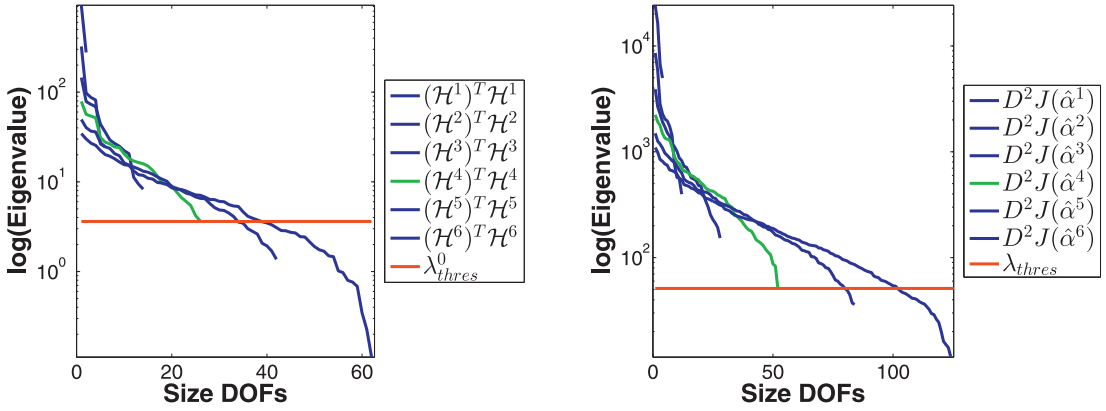

(a) Eigenvalues for the non-diffusion weighted data estimate (Step 3)

(b) Eigenvalues for MLFE (Step 6)

Fig. 17. Eigenvalue distribution for the Hessian matrices for IVL (real) data using $\sigma_\delta = 7.5$mm for patches refinement levels $1, \ldots, 6$ (left and right, respectively). Eigenvalue distribution used for threshold evaluation is highlighted with green. (For interpretation of the references to colour in this figure legend, the reader is referred to the web version of this article.)

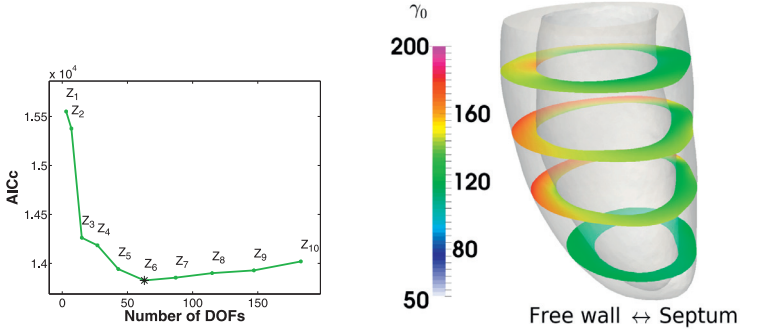

(a) AICc progression of non-weighted estimation

(b) Reconstructed non-diffusion weighted information γ^0

Fig. 18. Reconstruction of non-diffusion weighted data $g^{(0)}_1, \ldots, g^{(0)}_{N^{(0)}}$ for $\sigma_\delta = 7.5$mm. (a) AICc curve for patch refinements $\mathcal{Z}^1, \ldots, \mathcal{Z}^{10}$. Minimal value, used for the MLFE, is highlighted (black star). (b) Short axis cuts of the 3D-reconstruction $\boldsymbol{\gamma}^0$.

one without perturbation $\sigma_\delta = 0$mm and one with $\sigma_\delta = 7.5$mm. A comparative view of (EV) with both IVL data sets can be seen in Fig. 16. Analogously to Section 3.2 we register the binary masks of IVL data and left ventricular geometry onto each other. Then, the outlier detection scheme described in the same section is applied for the gray values of the non-diffusion weighted and diffusion weighted images.

4.3. Estimation results

The estimation results for the IVL data using the algorithm presented in Section 2.4 are now presented. The sequence of patches used here is already illustrated in Fig. 3, and the eigenvalue curves computed for the thresholds evaluation are presented in Fig. 17.

In Fig. 18 the AICc curve for the non-diffusion weighted estimation (Step 3 - Section 2.4), together with the three-dimensional reconstruction of the non-diffusion weighted data is depicted. Note that the systematic increase in the signal in the free-wall (compared to the septum), as it is noticeable in the original high resolution data in Fig. 16, is reconstructed satisfactorily. The computed AICc maps for both inspected cases are visualized in Fig. 19, while the endocardial and epicardial angle distributions are plotted schematically as bullseye maps in Fig. 20. Moreover, to quantify the loss of information due to the data reduction from the EV to the IVL data set, we re-perform the estimation with the high resolution data using the patch resolution following from the AICc analysis in the IVL case and denote it as “EV-equivalent”. The helix angle values at both endo- and epicardium vary between 70°/20° and −70°/−20°, respectively, however with different ranges. In the epicardium, the fibers get more vertical when moving from base to apex, and when moving from the posteroseptal to the anterior lateral regions. In the endocardium, this behavior changes: fibers get more vertical from the free wall to the septum, while the variation in the long-axis direction is less remarkable. These general characteristics confirm an important variability of the helix angle.

The estimated fibers of the MLFE having the minimal AICc value are shown in Fig. 21, for both $\sigma_\delta = 0$mm and $\sigma_\delta = 7.5$mm data. The fibers are colored by the angle between the fiber alignment resulting from the IVL and EV-equivalent analysis. As it can be appreciated, the main differences between IVL and EV-equivalent occur in the regions where few or no IVL-data is available, e.g. at the base and apex. Naturally, in both cases regions of lower differences are associated with the slices locations in the IVL data. Note also that angle differences between IVL-EV-equivalent are more homogeneously distributed in space due to the spread in the slice displacement attributed to motion. As it can also be appreci-

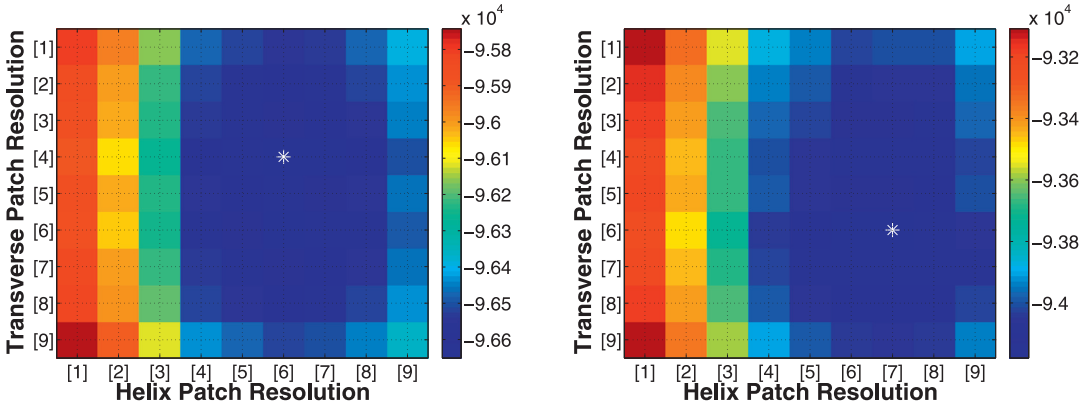

(a) AICc plot for MLE: $\sigma_\delta = 0$mm (b) AICc plot for MLE: $\sigma_\delta = 7.5$mm

Fig. 19. Computed AICc values for the in-vivo like data set. White star indicates the location of the minimum.

Table 3
Estimated spatially constant parameters and comparison with voxel-wise estimation.

	EV voxel	IVL - $\sigma_\delta = 0.0$mm	EV eq.	IVL - $\sigma_\delta = 7.5$mm	EV eq.
$\lambda_1[10^{-6}\frac{cm^2}{s}]$	9.45	9.19	9.45	9.18	9.46
$\lambda_2[10^{-6}\frac{cm^2}{s}]$	6.52	6.27	6.50	6.23	6.50
$\lambda_3[10^{-6}\frac{cm^2}{s}]$	5.48	$=\lambda_2$	$=\lambda_2$	$=\lambda_2$	$=\lambda_2$
β		−0.7	−0.42	−0.35	−0.38
$\sigma[10^{-2}]$		6.09	8.91	6.23	8.90

ated in Fig. 21(c), when analyzing the difference between IVL with $\sigma_\delta = 0$mm and $\sigma_\delta = 7.5$mm, both results differ in less than 10°, with few exceptions of around 20°.

Finally, the estimated spatially-constant parameters are presented in Table 3, for all two IVL estimations and their EV equivalents. For comparison, the mean diffusivities estimated voxelwise from the full data set are also indicated. Note that the fiber and cross-fiber diffusivities of model and voxelwise reference result in comparable ranges. The transmural variation of the helix angle is shown in Fig. 22, showing almost a linear behavior.

Finally, we include a comparison between MLFE and CLTI for the IVL data set with perturbed slices positions, see Fig. 23. We can clearly appreciate that the slices motion induces spurious fiber directions in the CLTI reconstruction (see fibers inside the black boxes), while the MLFE achieves in keeping them smooth. Moreover, it is also clear to see in general that the CLTI fibers are more horizontal than the reconstructed by the MLFE by analyzing the helix angles.

4.4. Results on a bi-ventricular geometry

We show now that our fiber estimation method can be extended to bi-ventricular cases. As it is well known, the subsampled in-vivo like data of the previous section does not permit to capture the transmural variations of the right ventricular fiber angles due to its reduced wall thickness compared with the voxel size. Therefore, we exemplify the bi-ventricular estimation on the full 3D ex-vivo data set only.

As done in the monoventricular case in the previous section, we run the bi-ventricular estimation with a fixed patch resolution, see Fig. 24(a), and we only perform the maximum likelihood estimation from Step 6. The reconstructed bi-ventricular fiber organization is shown in Fig. 24(b). In the left ventricle the fibers are colored by the angle difference between the EV-equivalent estimation from last section and the biventricular estimation. In general, the angle differences are under 10^o, which are most likely to appear due to the different patches used in both cases. Naturally, larger angle differences of 20^o to 25^o appear in the transition between the ventricles since the bi-ventricular rule-based model enforces a different fiber topology in this location. There, the fibers of the right ventricle smoothly interdigitate into fiber organization of the left ventricle, while in the monoventricular geometry the fibers are forced to be tangent to the left ventricular epicardium.

4.5. Comparison to the EV tensor data

Even though a ground truth fiber distribution is not available, we can assume that the fiber field closest to the true one is the first eigenvector of the high resolution 3D EV data. Hence, we can compare the fiber estimations of both CLTI and MLFE to this reference data set. To this end, we interpolate the fiber orientations of the EV tensor data, given by JHU, to the left ventricular domain and then compute the angle difference with respect to the MLFE and CLTI estimates. The results of this computation is depicted in Fig. 25. As it can be clearly noticed, the difference to the EV fiber field of the MLFE is significantly smaller than the CLTI. In fact, only at the endo- and epicardial surfaces and the apical area, bigger errors are noticeable. The remaining areas show angle differences smaller than 10°. Beware, that the differences at the endocardial region might respond to endocardial trabeculations, see the more perturbed fiber alignment at the endocardial area for the EV tensor data. These errors do not solely occur at the endo- and epicardial rim, but also throughout the left ventricular domain.

5. Discussion

5.1. Results for the synthetic data examples

For both synthetic examples, the maximum likelihood fiber estimator (MLFE) allowed a much more precise reconstruction of the fiber field than the state of the art, i.e. the curvilinear tensor interpolation method (CLTI), see Figs. 11–12. In particular, the impact of the misalignment and consequent registration errors in the MLFE

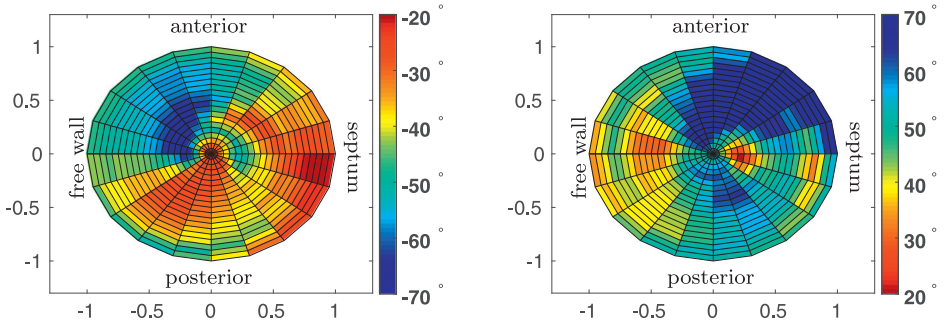

(a) $\sigma_\delta = 0$mm

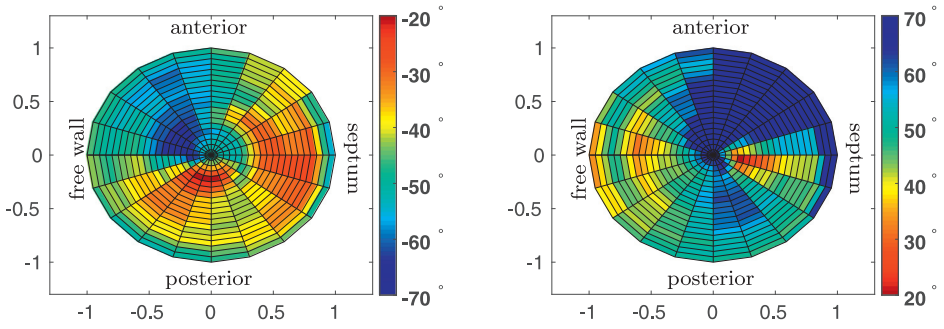

(b) EV equivalent $\sigma_\delta = 0$mm

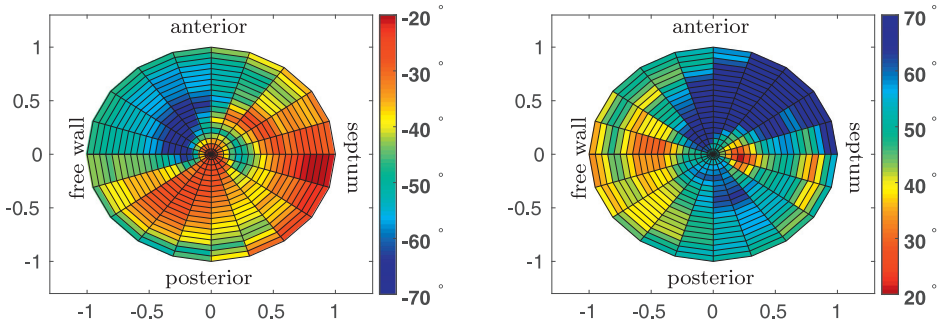

(c) $\sigma_\delta = 7.5$mm

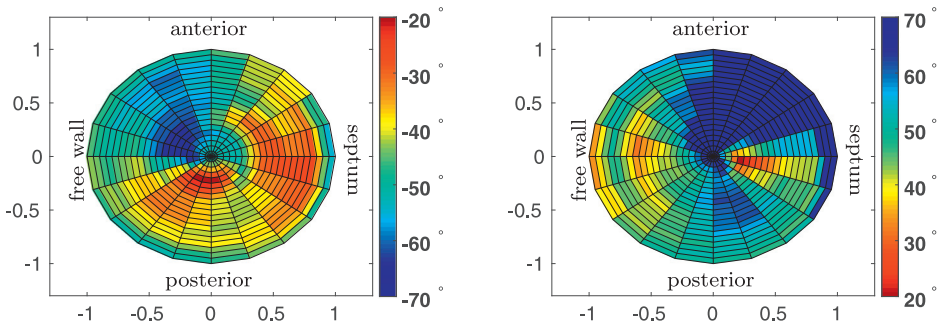

(d) EV equivalent $\sigma_\delta = 7.5$mm

Fig. 20. Bullseye plot for resulting helix angle for epicardial (left) and endocardial (right) ventricular surface.

are minimal, and depending on the regions they may even get improved (see Fig. 12). This is exactly what we intend with the MLFE. If the DWIs move, they basically obtain another measurements but from the same fiber family, making it robust to DWIs motions. In other words, MLFE "glues" the DWI information using the general knowledge that there are fiber bundles in the background. In contrast, the CLTI reconstruction quality is strongly compromised by motion artifacts. This feature of the MLFE may have an important impact in the DW-MRI acquisition, since the respiratory navigator acceptance window for in-vivo acquisitions can be considerably relaxed without compromising the fiber estimation accuracy. As a direct implication this may also allow the acquisition time to be

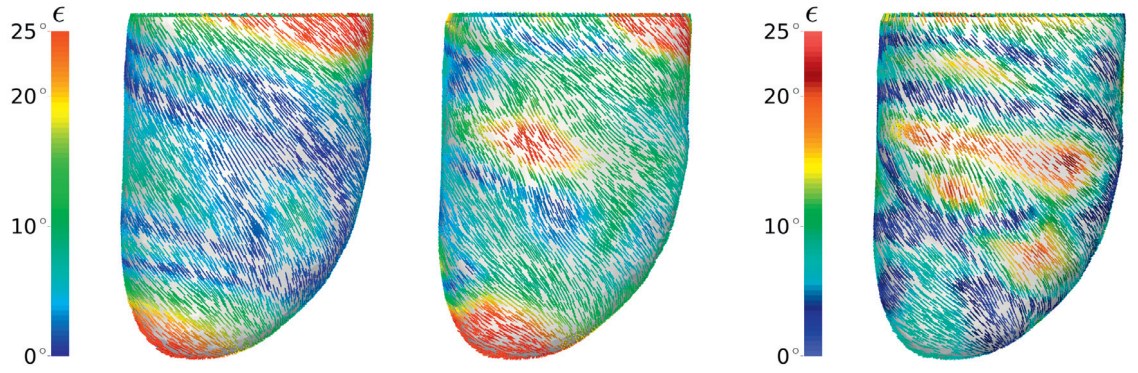

(a) $\sigma_\delta = 0$mm (b) $\sigma_\delta = 7.5$mm (c) Difference

Fig. 21. Resulting fiber organization colored by: (a)-(b) difference to respective ex-vivo data estimate, (c) difference angle between (a) and (b).

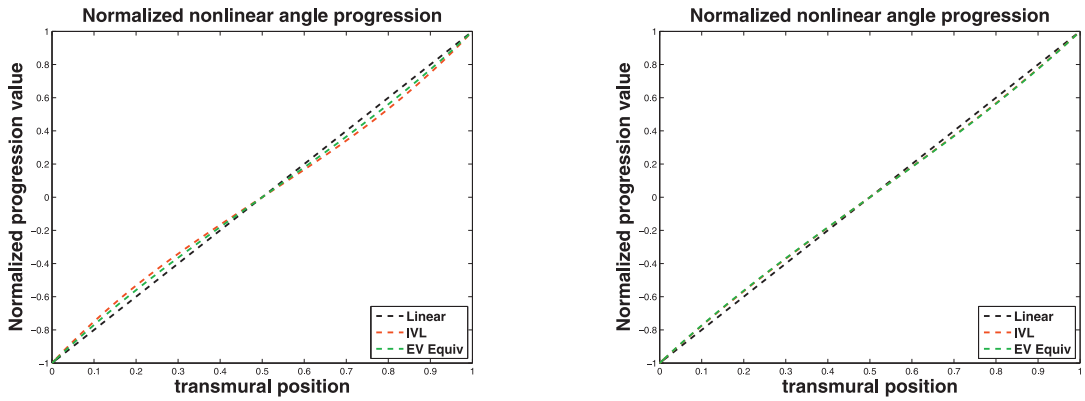

(a) $\sigma_\delta = 0$mm (b) $\sigma_\delta = 7.5$mm

Fig. 22. Resulting transmural helix angle variation for the four estimation cases detailed in Table 3. On the right side the green curve conceals the red one. (For interpretation of the references to colour in this figure legend, the reader is referred to the web version of this article.)

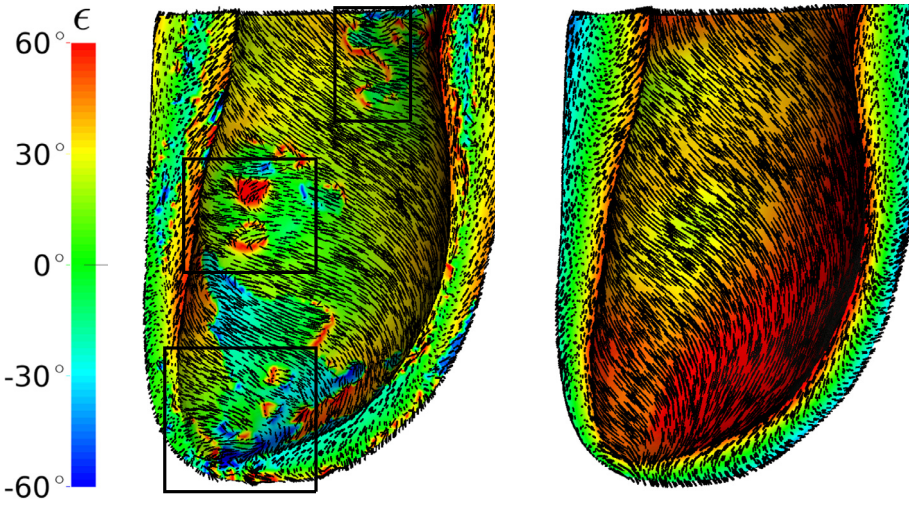

(a) CLTI $\sigma_\delta = 7.5$mm (b) MLFE $\sigma_\delta = 7.5$mm

Fig. 23. Estimated fiber organization for IVL data with $\sigma_\delta = 7.5$mm colored by helix angle. Black boxes focus on the spurious fiber oscillations.

substantially reduced and hence make cardiac fiber measurements feasible for clinical studies.

In practice, it is accepted that magnitude MRI signals have Rician distribution of the noise. The proposed estimator, as formulated through a nonlinear least-squares problem, assumes that the signal attenuation statistics are Gaussian for the sake of simplicity. We saw in the numerical examples that the Gaussian assumption allowed an excellent reconstruction of parameters and of the fibers even when we perturb the diffusion weighted images with considerable Rician noise.

We also would like to remark the advantages that the formulation as a maximum likelihood estimation provides. It not only

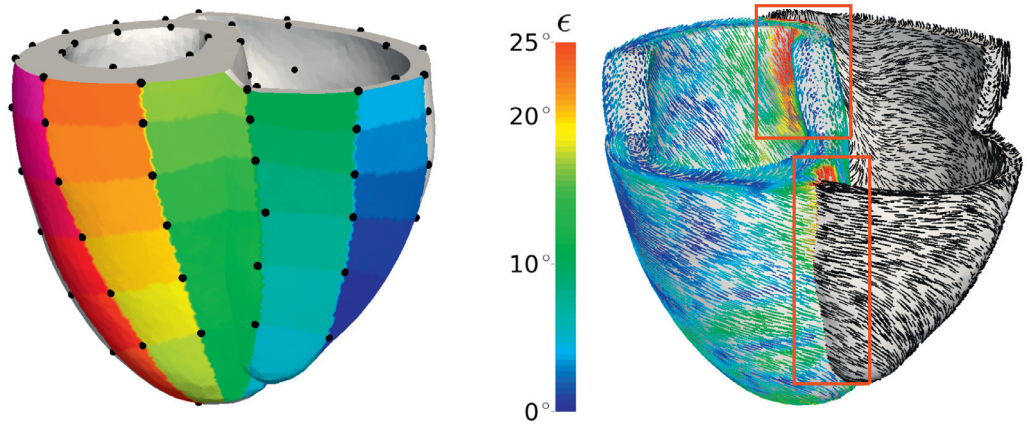

(a) Bi-ventricular patch structure (b) Estimated bi-ventricular fibers

Fig. 24. Bi-ventricular fiber estimation. Left: patch structure on the biventricular geometry. Right: estimated fibers, in the left ventricle colored by difference angle between mono- and biventricular cases. Transition of left to right ventricle is highlighted by the red boxes. (For interpretation of the references to colour in this figure legend, the reader is referred to the web version of this article.)

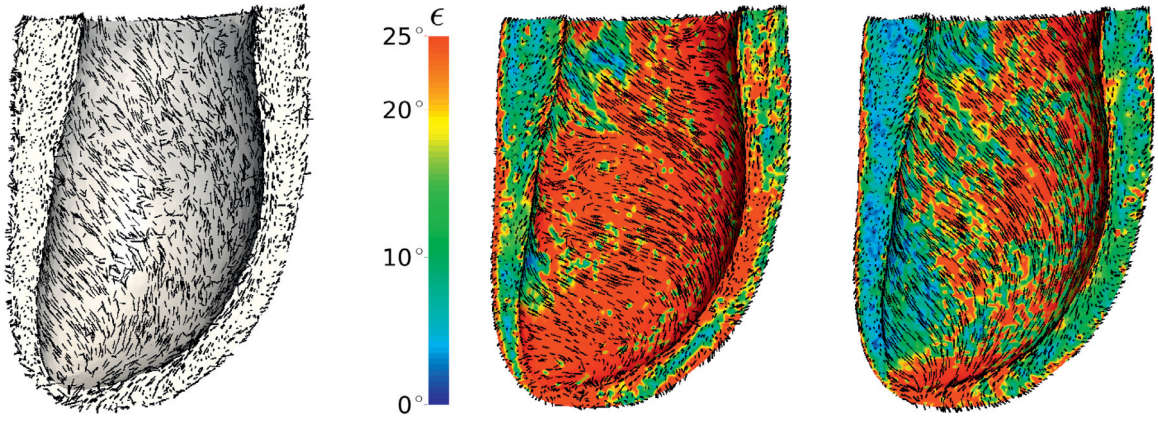

(a) EV fibers (b) CLTI fibers (c) MLFE fibers

Fig. 25. Comparison of EV fibers to the MLFE and CLTI using IVL $\sigma_\delta = 7.5$mm data. Colors in (b) and (c) correspond to the angle difference between the estimated and the EV fibers.

gives a robust way to reconstruct the data using general knowledge of the phenomena in question, like in this case the histological one, but also to take advantage of theoretically well founded tools in statistics, like the Akaike's information criteria. This allows to choose the parametrization of the model according to the amount and quality of the available data, hence avoiding under- or over-parametrization improving the estimation accuracy. Moreover, these tools help to identify systematic changes over random noise, by requiring larger amounts of degrees-of-freedom, like for example for the transverse angle in both synthetic cases and in the helix angle in the "perturbed" one.

5.2. Results for the real data example

For the sake of estimating the main fiber direction, the transverse isotropic diffusion tensor assumption in Equation (2) appears to be reasonable in an approach when analyzing the real data high resolution DW-MRI data set. The second and third mean diffusivities in the high resolution data are very close to each other ($6.52 \cdot 10^{-6}$ and $5.48 \cdot 10^{-6}$) compared to the first diffusivity ($9.45 \cdot 10^{-6}$). Of course, an extension to a fully anisotropic tensor would allow to differentiate the second and third directions. Our MLFE opens the door to perform systematic studies in larger, in-vivo data sets to study inter- and intra-specimen variability and to intend to detect perturbed dependencies for both helix and potentially sheet angle directions.

5.3. Computational aspects

Putting aside the segmentation of the myocardium and the DWIs registration, which will be the common processing procedure for all approaches, our current implementation of the MLFE requires in terms of computing time:

- For the generation of the interpolation operators for all patches, i.e. Step 1 in Section 2.4, it takes less than 15 minutes until a total number of $\Pi = 9$ patch level refinements on an Intel(R) Xeon(R) E5630 @ 2.53GHz, 12 GB RAM in a serial computation. Note that the generation of each column of the interpolation operators is independent of each other, therefore this time can still be reduced in a parallel framework.
- Once the linear operators are computed, several optimizations have to be run in order to find the patch combination that minimizes the AICc. In the examples of this manuscript, this part takes around 1–2 hours. It is noted that the AICc may be minimized sequentially for each variable and still achieving the same minimum, compare Figs. 10 and 20. This involves a complexity $\mathcal{O}(2\Pi)$ instead of $\mathcal{O}(\Pi^2)$, allowing the AICc optimization time to be reduced to some minutes.

Hence, the whole fiber estimation would take a computation time compatible with clinical practice and also negligible, when compared to large-scale cardiac bio- and multi-physical simulations. Of course, this outlook does not consider the potential improvements in hardware architecture.

5.4. Other approaches to estimate/extrapolate fiber data

Optimization of parametrized fiber models. Some cardiac fiber angle models have already been optimized using 3D-DW-MRI (ex-vivo) data. Calibration of a constant surface helix angle against DW-MRI data was done by sampling several helix angles and choosing the best fitting respective the first eigenvector (Bayer et al., 2012), or linear regression from helix angles computed from imaging data (Muñoz et al., 2010). This implies an over-regularization of the fiber field, like it is done in MLFE in $k = 1$ patch refinement level. Moreover, it also does not take into account the fact that diffusion information is non-directional, so the estimated fiber angles depend on the chosen convention for the fiber sign. Extending those works, in Nagler et al. (2013) we developed a parametrizable angle representation (similar to the one presented here), and the RBM fibers interpolated component-wise to the first eigenvector of the 3D-DW-MRI data.

The nonlinear estimation framework on a simple (non-deformed) ellipsoid geometry has been presented at a very preliminary stage (Nagler et al., 2015). In this work we have addressed the lack of studying for example the choice of the refinement level of the patches, introduction of regularization, and applicability on real DW-MRI with different types of slice misalignment. Therefore, the current manuscript represents a considerable improvement in terms of the methodology and extension of the results with respect to the preliminary works.

For the sake of completeness, alternative parametrization are the generalized helicoid model (Savadjiev et al., 2012) or the moving frames approach (Piuze et al., 2015).

For all of these approaches the start-point of analysis were the eigenvectors of a tensor per voxel, which is only available from co-existent and spatially aligned diffusion images in each voxel, and hence they optimize directly on the helix (and transverse) angles from the first eigenvector of the data. It is important to remark that doing so, the estimated angles depend on the chosen convention for the sign of the eigenvector. We remark that our approach is independent of this fact by construction. Moreover, we allow for sparsity of diffusion data, what none of such methods is able to handle.

Template-based methods. Some authors have proposed to reconstruct the fiber organization for arbitrarily geometries by morphing a high resolution ex-vivo DW-MRI data set (Sundar et al., 2006; Vadakkumpadan et al., 2012, 2013). Therefore the deformation field, gained via a registration of the template to a target geometry, is applied to the tensor information. Alternatively, statistical shape predictors were generated by correlating the geometry with respective fiber orientations (Lombaert and Peyrat, 2013; Lekadir et al., 2014). The correlation is performed using regression techniques applied to the geometry and fiber organization of a small ex-vivo DW-MRI data set. Based on the statistical shape model the fiber organization is determined for an arbitrary given domain. These approaches do not use specific diffusion measures of the specific heart, and rely on potential correlations of the shape and the fibers field. However, later in Lekadir et al. (2016), the authors introduced a way to additionally take advantage of multi-slice diffusion data measured on a specific patient.

Again, these approaches also rely on the spatial coexistence of the diffusion information by working directly with the eigenvectors of the diffusion tensors estimated voxel-wise. Moreover, the results may be biased through the training sample or template, which is also subjected to noise, and hence specific features of the measured fiber field in a specific patient may be blurred by the training set. Finally, it is important to remark that these family of algorithms need user interaction for the definition of a number of free parameters (e.g. six in Lekadir et al. (2016)).

In contrast to these techniques, the MLFE does not need any training set or definition of a priori values for the parameters, and hence are estimated using the patient-specific data only, avoiding biasing by the priors. Moreover, the MLFE is sensitive to one parameter only, the regularization threshold, which can take only few possible values that are easy to choose around a suggested value depending on the number of image slices (the maximum number of patches Π is purely instrumental for finding the AICc minimum, and $\varphi_{\max}$ has a fully physiological motivation).

5.5. Perspectives

Improvements of the MLFE-framework. The framework can be extended to the estimation of the sheet direction, by the analysis of experimental in-vivo and ex-vivo animal data sets, since inhomogeneities across the ventricle can be a marker for myocardial remodeling (Helm et al., 2006). Doing so, our framework can help to better understand the full cardiac fiber architecture in different patho-physiological states.

Concerning the algorithmic part, other parameterizations can be tested, for example different basis functions for the angles, gaussians and/or global polynomials. This would also have implications on the type of regularizations to be implemented. Ideally, an automatic choice of the regularization threshold or weighting (depending on the chosen parametrization strategy) could be developed in order to control a common model's output (for example, spatial derivatives of the reconstructed fiber angle field), in order to minimize the user interaction.

Another potential improvement of the MLFE is to allow for local DOF refinements depending on AICc values computed by ventricle region, instead of a global AICc/DOF relation as computed above.

We would also like to remark that the MLFE is capable to estimate the measurement noise level of the diffusion data. Notice also that due to coil geometry SNR is spatially varying, hence knowledge on spatial distribution of measurement noise can consequently be used in the MLFE framework for enhancing estimations.

Applications. The found helix angle variability in the real data example allows to study the effects of such variabilities in biophysical cardiac models (active/passive mechanics, electrophysiology). After an inter- and intra-specimen fiber angle variability study in larger heart samples, the fiber model presented can conveniently serve to consider these variabilities, since the location of the degrees-of-freedom are chosen using the same anatomical landmarks in each heart. Therefore, estimated fiber angles in one heart can be directly transferred to other geometries and the variability of biophysical simulation outputs can be easily studied. Alternatively, fiber angles can be directly "transferred" from other hearts, if diffusion measurements are not available.

The ability of the MLFE to handle arbitrarily spaced DWIs allows an increase of the reconstructed fiber precision for the same scan time, compared with previously reported algorithms. This flexibility of the choice of the diffusion encoding directions and slices may allow in the future to speed-up the acquisition of diffusion MR sequences. Moreover, due to the focus on the fiber direction the amount of diffusion encoding direction at a given accuracy might be reduced. Beyond that a study quantifying the influence of the amount of diffusion encoding directions, number of slices and other acquisition parameters onto the estimation result would

be an important step towards reducing the acquisition time. Moreover, this algorithmic flexibility of MLFE permits to include and directly compare data from different scan sessions, or from different magnetic fields strengths and estimating different noise levels.

Another benefit of the method is that it adapts to any shape of the heart, since we do not require to morph the left-ventricular shape onto a prolate spheroid, naturally allowing the study to pathological ventricular shapes.

Furthermore, another potential application is fibrosis detection. Excellent correlation between the signal decay and gadolinium enhanced images (Nguyen et al., 2015) has recently been shown. The MLFE can be used for example to differentiate healthy and fibrotic tissue, by estimating the spatial distribution of the eigenvalues of the diffusion tensor.

6. Summary and conclusions

We have presented a three-dimensional fiber reconstruction scheme, which can directly handle arbitrarily spaced diffusion weighted MR images. This allows for an increase of the reconstructed fiber precision for the same scan time, compared to previously reported algorithms. This flexibility of choice of the diffusion encoding directions and slice positions may allow to speed-up the acquisition of diffusion MR sequences in the future. Several applications can emerge from this new methodology for fully exploiting diffusion information in heart, enhancing non-invasive characterization of myocardial tissue properties.

Acknowledgements

The results presented in this article are part of the *Advanced Cardiac Mechanics Emulator*, an initiative supported by the Institute for Advanced Study (Technical University of Munich). This support is gratefully acknowledged. C. Bertoglio thanks also to the Conicyt Basal Program PFB-03 for partial support.

We also thank Jack Harmer (King's College London), Radomír Chabiniok (INRIA Saclay Île-de-France), Arun Tangirala (IIT Madras) and Felipe Tobar (U. Chile) for the valuable discussions. Thanks also goes to Martin Pfaller (Technical University of Munich) and David Nolte (U. Chile) for proofreading the manuscript.

Finally, thanks to Drs. Patrick A. Helm and Raimond L. Winslow at the Center for Cardiovascular Bioinformatics and Modelling and Dr. Elliot McVeigh at the National Institute of Health for provision of DW-MRI data.

Appendix A. Start value interpolation

To compute the starting value $\boldsymbol{\alpha}_0 = \mathcal{I}_{k_h,k_t}(\widehat{\boldsymbol{\alpha}}_{k_h-1,k_t}, \widehat{\boldsymbol{\alpha}}_{k_h,k_t-1}) = \left[\boldsymbol{\Theta}_0, \boldsymbol{\Phi}_0, \beta_0, \boldsymbol{\lambda}_0, \sigma_0\right]$ we will first define:

$$\left[\hat{\boldsymbol{\Theta}}_1, \hat{\boldsymbol{\Phi}}_1, \hat{\beta}_1, \hat{\boldsymbol{\lambda}}_1, \hat{\sigma}_1\right] = \widehat{\boldsymbol{\alpha}}_{k_h-1,k_t}$$

$$\left[\hat{\boldsymbol{\Theta}}_2, \hat{\boldsymbol{\Phi}}_2, \hat{\beta}_2, \hat{\boldsymbol{\lambda}}_2, \hat{\sigma}_2\right] = \widehat{\boldsymbol{\alpha}}_{k_h,k_t-1}$$

Then, we compute the starting value as

$$\left[\boldsymbol{\Theta}_0, \boldsymbol{\Phi}_0, \beta_0, \boldsymbol{\lambda}_0, \sigma_0\right] = \left[\mathcal{I}_{k_h}(\hat{\boldsymbol{\Theta}}_1), \mathcal{I}_{k_t}(\hat{\boldsymbol{\Phi}}_2), \frac{1}{2}\left(\hat{\beta}_1 + \hat{\beta}_2\right), \frac{1}{2}\left(\hat{\boldsymbol{\lambda}}_1 + \hat{\boldsymbol{\lambda}}_2\right), \frac{1}{2}\left(\hat{\sigma}_1 + \hat{\sigma}_2\right)\right]$$

where the operators $\mathcal{I}_{k_h}$ and $\mathcal{I}_{k_t}$ are identical to Step 3 of Section 2.4.

Appendix B. Reference fiber field

The synthetic geometry is first defined using the well known *prolate spheroid coordinates* given by the following parametrization

$$x(\mu, \nu, \phi) = f \sinh(\mu) \sin(\nu) \cos(\phi) \tag{B.1}$$

$$y(\mu, \nu, \phi) = f \sinh(\mu) \sin(\nu) \sin(\phi) \tag{B.2}$$

$$z(\mu, \nu, \phi) = f \cosh(\mu) \cos(\nu) \tag{B.3}$$

with f the *focus factor*, $\mu \in [\mu_1, \mu_2]$ the *wall-depth coordinate*, $\nu \in [90°, 180°]$ the *inclination angle* and ϕ the *rotation angle*. We compute the constants μ_1 (Endocardial surface), μ_2 (Epicardial surface) and the focus f by choosing a volume of V=130ml, a wall thickness of the ventricle at the base of d=7mm and a ventricular endocardial length diameter of b=90mm, which results in the cross section radius of a=$\sqrt{\frac{3V}{2\pi b}} \approx 26mm$, see schematic overview in Fig. 26(a). Using the relations

$$\text{Basal Endocardium: } x(\mu = \mu_1, \nu = 90°, \phi = 0°) = f \sinh(\mu_1) \stackrel{\text{def}}{=} a \tag{B.4}$$

$$\text{Basal Epicardium: } x(\mu = \mu_2, \nu = 90°, \phi = 0°) = f \sinh(\mu_2) \stackrel{\text{def}}{=} a + d \tag{B.5}$$

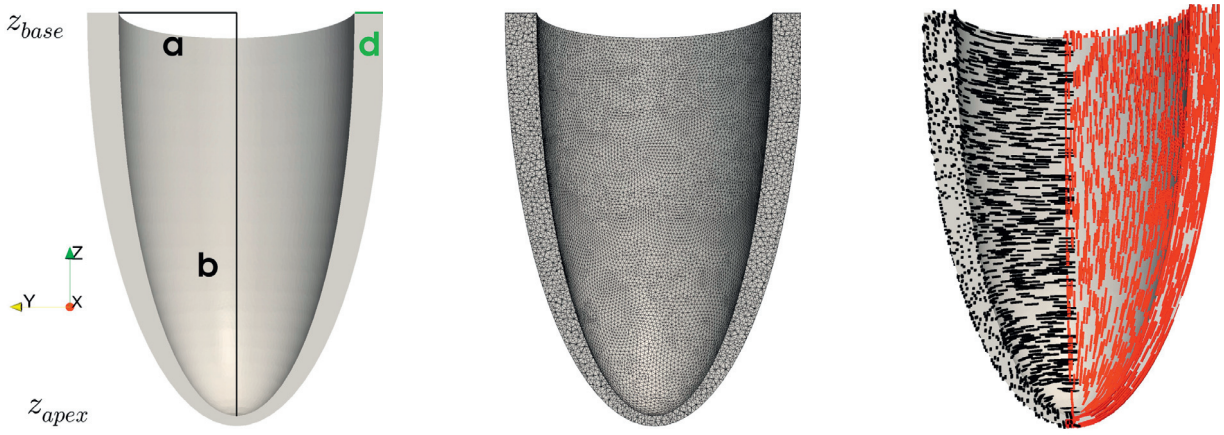

(a) Geometry (b) Mesh, $h = 0.9$ mm (c) Local basis vectors

Fig. 26. Descriptive overview of synthetic (a) prolate spheroid geometry, (b) generated mesh and (c) utilized local coordinate system g_1 (black) and g_2 (red). (For interpretation of the references to colour in this figure legend, the reader is referred to the web version of this article.)

Apical Endocardium: $z(\mu = \mu_1, \nu = 180^\circ) = f\cosh(\mu_1) \stackrel{\text{def}}{=} b$ (B.6)

we obtain $\mu_1 = \tanh^{-1}(\frac{a}{b}) \approx 0.3$, $f = \frac{a}{\sinh(\mu_1)} \approx 86.1$ and $\mu_2 = \sinh(\frac{a+d}{f}) \approx 0.38$

Using the surface parametric representation of the spheroid (B.1)-(B.3), we generated a surface and then a volumetric cartesian mesh using `GmsH` (Geuzaine and Remacle, 2009), see Fig. 26(b).

Note that for assigning the fibers (helix angles and local coordinate system) to the mesh nodes from formulas in Section 3.1, we also need the inverse transformation:

$$\mu(x,y,z) = \cosh^{-1}\left(\frac{1}{2f}\left(\sqrt{x^2+y^2+(z+f)^2} - \sqrt{x^2+y^2+(z-f)^2}\right)\right) \quad \text{(B.7)}$$

$$\nu(x,y,z) = \cos^{-1}\left(\frac{1}{2f}\left(\sqrt{x^2+y^2+(z+f)^2} - \sqrt{x^2+y^2+(z-f)^2}\right)\right) \quad \text{(B.8)}$$

$$\phi(x,y,z) = \text{atan2}(y,x) \quad \text{(B.9)}$$

References

Akaike, H., 1974. A new look at the statistical model identification. IEEE Trans. Autom. Control 19, 716–723.

Basser, P., Mattiello, J., LeBihan, D., 1994. Estimation of the effective self-diffusion tensor from the NMR spin echo. J. Magn. Reson. 103, 247–254.

Bayer, J., Blake, R., Plank, G., Trayanova, N., 2012. A novel rule-based algorithm for assigning myocardial fiber orientation to computational heart models. Ann. Biomed. Eng. 40, 2243–2254.

Branch, M.A., Coleman, T.F., Li, Y., 1999. A subspace, interior, and conjugate gradient method for large-scale bound-constrained minimization problems. SIAM J. Sci. Comput. 21, 1–23.

Burnham, K.P., Anderson, D.R., 2004. Multimodel inference: understanding AIC and BIC in model selection. Sociol. Method Res. 33, 261–304.

Byrd, R., Schnabel, R., Shultz, G., 1988. Approximate solution of the trust region problem by minimization over two-dimensional subspaces. Math. Program. 40, 247–263.

Byrd, R.H., Gilbert, J.C., Nocedal, J., 2000. A trust region method based on interior point techniques for nonlinear programming. Math. Program. 89, 149–185.

Byrd, R.H., Hribar, M.E., Nocedal, J., 1999. An interior point algorithm for large-scale nonlinear programming. SIAM J. Optim. 9, 877–900.

Cerqueira, M.D., Weissman, N.J., Dilsizian, V., Jacobs, A.K., Kaul, S., Laskey, W.K., Pennell, D.J., Rumberger, J.A., Ryan, T., Verani, M.S., et al., 2002. Standardized myocardial segmentation and nomenclature for tomographic imaging of the heart a statement for healthcare professionals from the cardiac imaging committee of the council on clinical cardiology of the american heart association. Circ. 105, 539–542.

Chen, J., Song, S.K., Liu, W., McLean, M., Allen, J.S., Tan, J., Wickline, S.A., Yu, X., 2003. Remodeling of cardiac fiber structure after infarction in rats quantified with diffusion tensor MRI. Am. J. Physiol. 285, H946–H954.

von Deuster, C., Stoeck, C., Genet, M., Atkinson, D., Kozerke, S., 2015. Spin echo versus stimulated echo diffusion tensor imaging of the in vivo human heart. Magn. Reson. Med.. In press

Ennis, D.B., Nguyen, T.C., Riboh, J.C., Wigström, L., Harrington, K.B., Daughters, G.T., Ingels, N.B., Miller, D.C., 2008. Myofiber angle distributions in the ovine left ventricle do not conform to computationally optimized predictions. J. Biomech. 41, 3219–3224.

Fernandez-Teran, M., Hurle, J., 1982. Myocardial fiber architecture of the human heart ventricles. Anat. Rec. 204, 137–147.

Gamper, U., Boesiger, P., Kozerke, S., 2007. Diffusion imaging of the in vivo heart using spin echoes–considerations on bulk motion sensitivity. Magn. Reson. Med. 57, 331–337.

Geuzaine, C., Remacle, J.F., 2009. Gmsh: a 3D finite element mesh generator with built-in pre- and post-processing facilities. Int. J. Numer. Methods Eng. 79, 1309–1331.

Gudbjartsson, H., Patz, S., 1995. The rician distribution of noisy MRI data. Magn. Reson. Med. 34, 910–914.

Harmer, J., Pushparajah, K., Toussaint, N., Stoeck, C.T., Chan, R., Atkinson, D., Razavi, R., Kozerke, S., 2013. In vivo myofibre architecture in the systemic right ventricle. Eur. Heart J. 34, 3640.

Helm, P.A., Younes, L., Beg, M.F., Ennis, D.B., Leclercq, C., Faris, O.P., McVeigh, E., Kass, D., Miller, M.I., Winslow, R.L., 2006. Evidence of structural remodeling in the dyssynchronous failing heart. Circ. Res. 98, 125–132.

Hsu, E.W., Muzikant, A.L., Matulevicius, S.A., Penland, R.C., Henriquez, C.S., 1998. Magnetic resonance myocardial fiber-orientation mapping with direct histological correlation. Am. J. Physiol. 274, H1627–H1634.

Hurvich, C.M., Tsai, C.L., 1989. Regression and time series model selection in small samples. Biom. 76, 297–307.

Jones, D., Horsfield, M., Simmons, A., 1999. Optimal strategies for measuring diffusion in anisotropic systems by magnetic resonance imaging. Magn. Reson. Med. 42, 515–525.

Klein, S., Staring, M., Murphy, K., Viergever, M., Pluim, J., 2010. Elastix: a toolbox for intensity-based medical image registration. IEEE Trans. Med. Imag. 29, 196–205.

Lekadir, K., Hoogendoorn, C., Pereanez, M., Albà, X., Pashaei, A., Frangi, A.F., 2014. Statistical personalization of ventricular fiber orientation using shape predictors. IEEE Trans. Med. Imag. 33, 882–890.

Lekadir, K., Lange, M., Zimmer, V.A., Hoogendoorn, C., Frangi, A.F., 2016. Statistically–driven 3D fiber reconstruction and denoising from multi-slice cardiac dti using a markov random field model. Med. Imag. Anal. 27, 105–116.

Lieberman, C., Fidkowski, K., Willcox, K., van Bloemen Waanders, B., 2013. Hessian-based model reduction: large-scale inversion and prediction. Int. J. Numer. Methods Fluids 71, 135–150.

Lombaert, H., Peyrat, J., Croisille, P., Rapacchi, S., Fanton, L., Cheriet, F., Clarysse, P., Magnin, I., Delingette, H., Ayache, N., 2012. Human atlas of the cardiac fiber architecture: study on a healthy population. IEEE Trans. Med. Imag. 31, 1436–1447.

Lombaert, H., Peyrat, J.M., 2013. Joint statistics on cardiac shape and fiber architecture. In: Medical Image Computing and Computer-Assisted Intervention–MICCAI 2013. Springer, pp. 492–500.

MATLAB, 2013. Version 8.2.0.701 (R2013b). The MathWorks Inc., Natick, Massachusetts.

Moulin, K., Croisille, P., Feiweier, T., Delattre, B.M., Wei, H., Robert, B., Beuf, O., Viallon, M., 2015. In vivo free-breathing DTI & IVIM of the whole human heart using a real-time slice-followed SE-EPI navigator-based sequence: a reproducibility study in healthy volunteers. J. Cardiovasc. Magn. Reson. 17, P383.

Muñoz, E., Cárdenes, R., Frangi, A.F., 2010. Analysis of the Helix and Transverse Angles of the Muscle Fibers in the Myocardium Based on Diffusion Tensor Imaging. In: Engineering in Medicine and Biology Society (EMBC), 2010 Annual International Conference of the IEEE, pp. 5720–5723.

Nagler, A., Bertoglio, C., Gee, M., Wall, W.A., 2013. Personalization of cardiac fiber orientations from image data using the unscented kalman filter. In: Ourselin, S., Rueckert, D., Smith, N. (Eds.), Proceedings Functional Imaging and Modeling of the Heart: 7th International Conference, FIMH 2013, London, UK, June 20–22, 2013. Springer Berlin Heidelberg, Berlin, Heidelberg, pp. 132–140.

Nagler, A., Bertoglio, C., Ortiz, M., Wall, W.A., 2016. A spatially varying mathematical representation of the biventricular cardiac fiber architecture. Technical Report. Institute for Computational Mechanics, Technische Universität München; Center for Mathematical Modeling, Universidad de Chile. URL https://hal.inria.fr/hal-01280501.

Nagler, A., Bertoglio, C., Stoeck, C.T., Kozerke, S., Wall, W.A., 2015. Cardiac fibers estimation from arbitrarily spaced diffusion weighted MRI. In: van Assen, H., Bovendeerd, P., Delhaas, T. (Eds.), Proceedings Functional Imaging and Modeling of the Heart: 8th International Conference, FIMH 2015, Maastricht, The Netherlands, June 25–27, 2015. Springer Berlin Heidelberg, pp. 198–206.

Nguyen, C., Fan, Z., Sharif, B., He, Y., Dharmakumar, R., Berman, D.S., Li, D., 2013. In vivo three-dimensional high resolution cardiac diffusion-weighted MRI: a motion compensated diffusion-prepared balanced steady-state free precession approach. Magn. Reson. Med. 72, 1257–1267.

Nguyen, C.T., Lu, M., Fan, Z., Bi, X., Kellman, P., Zhao, S., Li, D., 2015. Contrast-free detection of myocardial fibrosis in hypertrophic cardiomyopathy patients with diffusion-weighted cardiovascular magnetic resonances. J. Cardiovasc. Magn. Reson. 17, 1–7.

Nielles-Vallespin, S., Mekkaoui, C., Gatehouse, P., Reese, T.G., Keegan, J., Ferreira, P.F., Collins, S., Speier, P., Feiweier, T., Silva, R., Jackowski, M.P., Pennell, D.J., Sosnovik, D.E., Firmin, D., 2013. In vivo diffusion tensor MRI of the human heart: reproducibility of breath-hold and navigator-based approaches. Magn. Reson. Med. 70, 454–465.

Piuze, E., Sporring, J., Siddiqi, K., 2015. Maurer–Cartan forms for fields on surfaces: application to heart fiber geometry. IEEE Trans. Pattern Anal. Mach. Intell. 37, 2492–2504.

Sachs, T.S., Meyer, C.H., Hu, B.S., Kohli, J., Nishimura, D.G., Macovski, A., 1994. Real-time motion detection in spiral MRI using navigators. Magn. Reson. Med. 32, 639–645.

Savadjiev, P., Strijkers, G.J., Bakermans, A.J., Piuze, E., Zucker, S.W., Siddiqi, K., 2012. Heart wall myofibers are arranged in minimal surfaces to optimize organ function. Proc. Natl. Acad. Sci. 109, 9248–9253.

Scollan, D., Holmes, A., Winslow, R., Forder, J., 1998. Histological validation of myocardial microstructure obtained from diffusion tensor magnetic resonance imaging. Am. J. Physiol. 275, H2308–H2318.

Stejskal, E., Tanner, J., 1965. Spin diffusion measurements: spin echoes in the presence of a time-dependent field gradient. J. Chem. Phys. 42, 288–292.

Stoeck, C.T., von Deuster, C., Genet, M., Atkinson, D., Kozerke, S., 2015. Second-order motion-compensated spin echo diffusion tensor imaging of the human heart. Magn. Reson. Med.. In press

Stoeck, C.T., Kalinowska, A., von Deuster, C., Harmer, J., Chan, R.W., Niemann, M., Manka, R., Atkinson, D., Sosnovik, D.E., Mekkaoui, C., Kozerke, S., 2014. Dual-phase cardiac diffusion tensor imaging with strain correction. PLoS ONE 9, e107159.

Streeter, D., 1979. Gross morphology and fiber geometry of the heart. In: Handbook of Physiology. Williams & Wilkins, pp. 61–112.

Streeter, D.D., Bassett, D.L., 1966. An engineering analysis of myocardial fiber orientation in pig's left ventricle in systole. Anat. Rec. 155, 503–511.

Streeter, D.D., Spotnitz, H.M., Patel, D.P., Ross, J., Sonnenblick, E.H., 1969. Fiber orientation in the canine left ventricle during diastole and systole. Circ. Res. 24, 339–347.
Sundar, H., Shen, D., Biros, G., Litt, H., Davatzikos, C., 2006. Estimating myocardial fiber orientations by template warping. In: 3rd IEEE International Symposium on Biomedical Imaging: Nano to Macro, 2006., pp. 73–76.
Toussaint, N., Stoeck, C.T., Schaeffter, T., Kozerke, S., Sermesant, M., Batchelor, P., 2013. In vivo human cardiac fibre architecture estimation using shape-based diffusion tensor processing. Med. Imag. Anal. 17, 1243–1255.
Upton, G., Cook, I., 1996. Understanding Statistics. OUP Oxford.
Vadakkumpadan, F., Arevalo, H., Ceritoglu, C., Miller, M., Trayanova, N., 2012. Image-based estimation of ventricular fiber orientations for personalized modeling of cardiac electrophysiology. IEEE Trans. Med. Imag. 31, 1051–1060.
Vadakkumpadan, F., Arevalo, H., Trayanova, N.A., 2013. Patient-specific modeling of the heart: estimation of ventricular fiber orientations. J. Vis. Exp. e50125.
Waltz, R., Morales, J., Nocedal, J., Orban, D., 2006. An interior algorithm for nonlinear optimization that combines line search and trust region steps. Math. Program. 107, 391–408.